Monthly Notices
of the
ROYAL ASTRONOMICAL SOCIETY

MNRAS **481,** 3623–3642 (2018)
Advance Access publication 2018 July 4

doi:10.1093/mnras/sty1754

On the observational diagnostics to separate classical and disk-like bulges

Luca Costantin,[1]★ E. M. Corsini,[1,2] J. Méndez-Abreu,[3,4] L. Morelli,[1,2,5] E. Dalla Bontà[1,2] and A. Pizzella[1,2]

[1]*Dipartimento di Fisica e Astronomia 'G. Galilei', Università di Padova, vicolo dell'Osservatorio 3, I-35122 Padova, Italy*
[2]*INAF – Osservatorio Astronomico di Padova, vicolo dell'Osservatorio 5, I-35122 Padova, Italy*
[3]*Instituto de Astrofísica de Canarias, Calle Vía Láctea s/n, E-38200 La Laguna, Tenerife, Spain*
[4]*Departamento de Astrofísica, Universidad de La Laguna, Calle Astrofísico Francisco Sánchez s/n, E-38205 La Laguna, Tenerife, Spain*
[5]*Instituto de Astronoma y Ciencias Planetarias, Universidad de Atacama, Copiapó, Chile*

Accepted 2018 June 27. Received 2018 June 27; in original form 2018 April 20

ABSTRACT

Flattened bulges with disk-like properties are considered to be the end product of secular evolution processes at work in the inner regions of galaxies. On the contrary, classical bulges are characterized by rounder shapes and thought to be similar to low-luminosity elliptical galaxies. We aim at testing the variety of observational diagnostics which are commonly adopted to separate classical from disk-like bulges in nearby galaxies. We select a sample of eight unbarred lenticular galaxies to be morphologically and kinematically undisturbed with no evidence of other components than bulge and disk. We analyse archival data of broad-band imaging from SDSS and integral-field spectroscopy from the ATLAS^{3D} survey to derive the photometric and kinematic properties, line-strength indices, and intrinsic shape of the sample bulges. We argue that the bulge Sérsic index is a poor diagnostics to discriminate different bulge types. We find that the combination of line strength with either kinematic or photometric diagnostics does not provide a clear separation for half of the sample bulges. We include, for the first time, the intrinsic three-dimensional shape of bulges as a possible discriminant of their nature. All bulges turn out to be thick oblate spheroids, but only one has a flattening consistent with that expected for outer disks. We conclude that bulge classification may be difficult even adopting all observational diagnostics proposed so far and that classical and disk-like bulges could be more confidently identified by considering their intrinsic shape.

Key words: galaxies: bulges – galaxies: formation – galaxies: fundamental parameters – galaxies: kinematics and dynamics - galaxies: photometry – galaxies: structure.

1 INTRODUCTION

The term *bulge* entered the vocabulary of extragalactic astrophysics in the early 1940s when Edwin Hubble, debating about the direction of rotation of spiral galaxies, denominated their central protuberances as nuclear bulges (Hubble 1943). This word was beyond doubt referred to as an observed structure sticking out from the galactic plane of lenticular and spiral galaxies. Later, the term also assumed a more physical meaning related to the processes driving the formation and evolution of galaxies. For example, Renzini (1999) looked at bulges as elliptical galaxies surrounded by an outer disk or, conversely, considered elliptical galaxies as bulges that somehow were not able to acquire and preserve a disk component.

Several operative definitions were proposed to outline the bulge component by analyzing the surface brightness distribution of the host galaxy. Kent (1986) pointed out that the galaxy isophotes in the bulge region are more round than those measured in the disk region, assuming that both bulge and disk have elliptical isophotes of constant but different axial ratios; but this diagnostics does not work for axisymmetric bulges seen face-on. Carollo, Ferguson & Wyse (1999) defined bulges as the inner components of galaxies whose light contribution exceeds the inward extrapolation of the exponential disc, with the advantage of dealing with all disc galaxies regardless of their inclination. The recent generalization of multicomponent photometric decompositions have led to define bulges as the central brightest component following a Sérsic profile (Méndez-Abreu et al. 2017).

The current picture divides galactic bulges into two broad classes, namely the *classical bulges* and *disk-like bulges*, according to their different formation processes (Athanassoula 2005). Classical bulges form via dissipative collapse of protogalactic gas clouds (Eggen, Lynden-Bell & Sandage 1962) or grow out of disc material triggered by satellite accretion during galaxy mergers (Aguerri, Bal-

★ E-mail: luca.costantin@studenti.unipd.it

cells & Peletier 2001; Hopkins et al. 2009). But, they could also grow by the coalescence of giant clumps in primordial disks (Bournaud 2016). Thus, these systems are expected to present hot orbits for their stars, having shapes that resemble elliptical galaxies and being intrinsically less flat than their surrounding disks. By contrast, disc-like bulges are thought to be the product of secular processes driven by internal processes in galaxies, responsible to rearrange energy and mass in their centre (Kormendy & Kennicutt 2004; Kormendy 2016). Due to their discy nature, these bulges are expected to preserve the intrinsic flatness of the original disc as well as its cold orbits. We choose to refer to disc-like bulges rather than to *pseudobulges* to avoid misinterpretations. Kormendy (1993) introduced the notion of *bulge-like discs* in the framework of a relaxed universe, when slow secular processes drive the evolution of galaxies rather than mergers. A decade later, Kormendy & Kennicutt (2004) renamed these objects as pseudobulges. Nowadays, the term pseudobulge is adopted to describe a wide assortment of bulge types ranging from boxy/peanut-shaped structures, which are actually bars seen from particular viewing angles (e.g. Laurikainen, Salo & Buta 2005; Méndez-Abreu et al. 2008b; Erwin & Debattista 2017), to those characterized by the presence of inner components, like ovals, nuclear bars, or disks, rings, dust lanes, and spiral arms (Fisher & Drory 2010), to bulges with a fainter surface brightness compared to elliptical galaxies of the same size (Gadotti 2009).

A proper classification of bulges based on their formation scenarios is highly desirable, although yet premature. Nevertheless, given the variety of formation processes, different photometric, kinematic, and stellar population properties are thought to differentiate different formation paths in bulges. Recently, Fisher & Drory (2016) have extended the early classification scheme by Kormendy & Kennicutt (2004) by reviewing the bulge properties, providing an updated list of observational criteria to classify classical and disk-like bulges, and addressing their demography in nearby galaxies. In this paper, we homogeneously apply all these criteria to a well-defined sample of bulges to investigate which one, or which combination of them, is more effective characterizing classical and disk-like bulges. Indeed, one or few of the criteria given by Fisher & Drory (2016) are commonly adopted to classify bulges (e.g. Fernández Lorenzo et al. 2014; Vaghmare et al. 2015; Mishra, Wadadekar & Barway 2017). However, even though this view divides bulges into well-defined classes, the complexity of galaxy formation suggests a continuity rather than a bimodality of bulge properties. Therefore, this picture could be reframed in term of the bulge intrinsic shape, where bulges are sorted from more to less flattened systems, as well as elliptical galaxies are classified on the Hubble tuning fork. In this context, boxy/peanut structures represent a separate or a related case of interest. Furthermore, the coexistence of composite bulges in the same galaxy leads to a more complicated picture and poses more challenges in galaxy formation mechanisms (Méndez-Abreu et al. 2014; Erwin et al. 2015). Thus, to preserve the original distinction of bulges according to their formation mechanisms, the bulge intrinsic shape could be useful to unveil the information on bulge orbits and evolutionary processes, from classical to disk-like systems. Moreover, we also propose to characterize the bulge intrinsic shape, which it is a diagnostics not yet adopted in bulge classification, in order to study its actual interplay with other bulge diagnostics. To address this issue, we select our sample bulges from the volume-limited ATLAS^{3D} survey of early-type galaxies (ETGs, Cappellari et al. 2011). It opened a new era for the integral-field spectroscopic surveys of nearby galaxies by solving some of the long-standing puzzles about the kinematic peculiarities (Krajnović et al. 2011), dynamical status (Emsellem et al. 2011), and stellar populations (McDermid et al. 2015) of ETGs (see also Cappellari 2016, for a review). On the other hand, we benefit from the ATLAS^{3D} legacy of two-dimensional maps of ionized-gas (Sarzi et al. 2013), stellar kinematics (Emsellem et al. 2011), and line-strength indices (Scott et al. 2013) to accurately measure the properties of our sample bulges in a consistent way.

The paper is organized as follows. We list the observational criteria for classifying bulges in Section 2. We present the galaxy sample in Section 3. We analyse the surface brightness distribution of the sample galaxies in Section 4. We recover the intrinsic shape of the sample bulges in Section 5. We analyse the stellar kinematics and line-strength indices of the sample bulges in Section 6. We investigate whether our bulges follow the same scaling relations traced by elliptical galaxies and large bulges in Section 7. We discuss the classification of the sample bulges in Section 8. We present our conclusions in Section 9.

2 OBSERVATIONAL CRITERIA FOR BULGE CLASSIFICATION

In their review about the properties and classification of bulges in nearby galaxies, Fisher & Drory (2016) proposed a number of observational criteria (i.e. category I diagnostics) that allow to mark a relatively clean separation between classical and disk-like bulges and to statistically classify all the bulges within a sample. They also identified other observational properties (i.e. category II diagnostics) that can be used to classify single bulges, but cannot be applied to the whole bulge population. Finally, they gave a few additional criteria (i.e. category III diagnostics), which are supposed to be necessary (but not sufficient) to identify a bulge as classical. Here, we provide a summary of the observational criteria given by Fisher & Drory (2016) grouped according to their category.

Classical bulges are thought to:

(1) $(\text{I-1})_{\text{C}}$ show no spiral or ring structures in the region where they dominate the galaxy light, as shown by optical images taken at high spatial resolution ($FWHM_{\text{PSF}} < 100$ pc);
(2) $(\text{I-2})_{\text{C}}$ have Sérsic index $n > 2$;
(3) $(\text{I-3})_{\text{C}}$ show Mg_b– σ and Mg_b–Fe_{5015} correlations consistent with those of elliptical galaxies;
(4) $(\text{I-4})_{\text{C}}$ have a strongly peaked radial profile of stellar velocity dispersion σ, with a gradient $\text{dlog}(\sigma)/\text{dlog}(r) < -0.1$ within $[r_{\text{min}}, r_{25\,\text{per cent}}]$, where $r_{\text{min}} = FWHM_{\text{PSF}}$ to exclude the inner regions of the kinematic maps which are most affected by blurring effects of the point spread function (PSF) and $r_{25\,\text{per cent}}$ is the radius where the surface brightness contribution of the bulge exceeds that of the disk by 25 per cent;
(5) $(\text{II-1})_{\text{C}}$ have central velocity dispersion $\sigma_0 > 130\,\text{km s}^{-1}$;
(6) $(\text{III-1})_{\text{C}}$ be consistent with the fundamental plane relation (FPR) of elliptical galaxies;
(7) $(\text{III-2})_{\text{C}}$ show low specific star formation rate $sSFR < 10^{-11}$ yr^{-1} (but this is not applicable to lenticular galaxies; Kormendy 2016);
(8) $(\text{III-3})_{\text{C}}$ rarely present extremely blue colours (e.g. $B - V < 0.65$).

Disk-like bulges are supposed to:

(1) $(\text{I-1})_{\text{D}}$ show spiral or ring structures in the region where they dominate the galaxy light, as shown by optical images taken at high spatial resolution ($FWHM_{\text{PSF}} < 100$ pc);
(2) $(\text{I-2})_{\text{D}}$ have Sérsic index $n < 2$;

(3) $(\text{I-3})_{\text{D}}$ show line-strength offset $\Delta\text{Mg}_b < 0.7$ Å compared to the $\text{Mg}_b - \sigma$ correlation, or $\Delta\text{Mg}_b < 0.7$ Å compared to the Mg_b–Fe_{5015} relation of elliptical galaxies;

(4) $(\text{I-4})_{\text{D}}$ present a stellar velocity dispersion radial profile that satisfies $\text{dlog}(\sigma)/\text{dlog}(r) > -0.1$ or $\langle v^2\rangle/\langle\sigma^2\rangle \geq 0.35$ within $[r_{\text{min}}, r_{25\,\text{per cent}}]$;

(5) $(\text{II-1})_{\text{D}}$ be low surface-brightness outliers in the Kormendy relation (KR) of elliptical galaxies;

(6) $(\text{II-2})_{\text{D}}$ present high specific star formation rate $sSFR > 10^{-11}$ yr^{-1} (but this is not applicable to lenticular galaxies; Kormendy 2016);

(7) $(\text{II-3})_{\text{D}}$ have line-strength indices $\text{Fe}_{5015} < 3.95$ Å and $\text{Mg}_b < 2.35$ Å;

(8) $(\text{II-4})_{\text{D}}$ be low-σ outliers in the Faber–Jackson relation (FJR) of elliptical galaxies;

(9) $(\text{II-5})_{\text{D}}$ show blue optical colours (e.g. $B - V < 0.5$).

It is worth noting that, even if the different observational properties of bulges can be explained in terms of formation process and evolutionary history, most of the above criteria are based on an *a priori* separation between classical and disk-like bulges which is usually done with a visual morphological classification. For these reasons, different authors (e.g. Graham & Worley 2008; Méndez-Abreu et al. 2018a) challenged these criteria by pointing out that they can easily lead to misclassification when one or few of them are adopted to select a particular type of bulge.

3 SAMPLE SELECTION

We selected our sample of unbarred lenticular galaxies among the nearby ETGs of the ATLAS^{3D} survey (Cappellari et al. 2011). Since this pilot project aims to understand the interplay of different bulge diagnostics, the sample galaxies were selected having in mind the simplest systems in terms of their structure, morphology, photometric and kinematic properties, that is, lenticular galaxies. ATLAS^{3D} provided the ideal starting point to challenge all the observational diagnostics proposed so far, where recent surveys like Calar Alto Legacy Integral Field Area (CALIFA) lack in spatial resolution to perform an exhaustive analysis for later Hubble type galaxies.

First, we considered the 111 galaxies classified as unbarred lenticular galaxies combining the information from Cappellari et al. (2011, Hubble stage) and Krajnović et al. (2011, barredness), since they are supposed to be the disk galaxies with the simplest structure having only a bulge and a disk component. Then, we examined only the 58 galaxies without any morphological or kinematic peculiarity. Indeed, we rejected all the galaxies with signatures of interaction or merging, as it results from the visual inspection of their Sloan Digital Sky Survey (SDSS) images and those with a kinematically distinct cores or counter-rotating components (McDermid et al. 2006; Krajnović et al. 2011). Finally, we restricted our analysis to the 22 galaxies with an inclination $\theta_\epsilon = \arccos(1-\epsilon) = [30^\circ, 60^\circ]$, derived from the axial ratio calculated from the global ellipticity measured within ∼3 effective radii of the galaxy in Krajnović et al. (2011) and assuming an infinitesimally thin disk. This is required to perform a successful photometric decomposition of the galaxy images. This sample was further curbed after performing the photometric decomposition of the SDSS images (see Table 1 and Section 4 for details). We found that (i) three galaxies turned out to be ellipticals rather than lenticulars, (ii) five galaxies had a bar and/or spiral arms, and (iii) six galaxies were too much inclined.

The final sample is composed of eight galaxies, for which we report the main properties in Table 2.

Table 1. Galaxies rejected after the photometric decomposition.

Galaxy (1)	Motivation (2)	Galaxy (3)	Motivation (4)
IC 3631	morph.	NGC 4474	inc.
NGC 525	inc.	NGC 4638	inc.
NGC 2577	inc.	NGC 5273	morph.
NGC 2685	inc.	NGC 5485	ell.
NGC 3648	morph.	NGC 6278	morph.
NGC 3665	ell.	PGC 35754	ell.
NGC 4379	morph.	UGC 9519	inc.

Notes. Columns (1), (3): galaxy name. Columns (2), (4): motivation for rejecting the galaxy; ell. = elliptical galaxy, morph. = bar and/or spiral arms, and incl. = too highly inclined galaxy.

4 SURFACE PHOTOMETRY

4.1 SDSS imaging

We retrieved the *i*-band images of the sample galaxies from the Data Archive Server (DAS) of the SDSS Data Release 9 (Ahn et al. 2012). All the archive images were already bias subtracted, flat-field-corrected, sky-subtracted, and flux-calibrated according to the associated calibration information stored in the DAS.

We made use of the procedure described in Pagotto et al. (2017) to measure the level of the sky background and its standard deviation (Table 3) after masking foreground stars, nearby and background galaxies, residual cosmic rays, and bad pixels. We found that our estimates of the sky background are systematically lower by 0.3 per cent than those given by SDSS and we applied such a correction to the images. We trimmed the sky-subtracted images to reduce the computing time when performing the photometric decomposition. We centred each galaxy in a field of view of at least 300×300 pixels^2 corresponding to 120×120 arcsec^2. Finally, we modelled the PSF of the resulting images with a circular Moffat function (Moffat 1969) with the shape parameters measured directly from the field stars (Table 3).

We fitted elliptical isophotes to the galaxy images with the `ellipse` task in IRAF[1] (Jedrzejewski 1987) after masking out as much as possible dust patches and lanes. We thus derived the radial profiles of azimuthally averaged surface brightness μ, ellipticity ε, and position angle *PA* to be used in the two-dimensional photometric decomposition to estimate the starting guesses of the galaxy structural parameters.

4.2 Photometric decomposition

We performed the two-dimensional photometric decomposition of the SDSS images of the 22 unbarred lenticular galaxies taken from the ATLAS^{3D} survey with no morphological and kinematic peculiarities and seen at intermediate inclination using the GAlaxy Surface Photometry 2-Dimensional decomposition algorithm (GASP2D; Méndez-Abreu et al. 2008a, 2014). We derived the structural parameters of each galaxy assuming that its surface brightness distribution was the sum of a Sérsic bulge (Sérsic 1968) and a double-exponential disk (Pohlen & Trujillo 2006), as described in Méndez-Abreu et al. (2017). We assumed the isophotes of the bulge and

[1]Image Reduction and Analysis Facility is distributed by the National Optical Astronomy Observatory (NOAO), which is operated by the Association of Universities for Research in Astronomy (AURA), Inc. under cooperative agreement with the National Science Foundation.

Table 2. Properties of the sample galaxies.

Galaxy	RA	DEC	d	scale	m_i	M_i	$R_{\rm e,\,gal}$	θ_ε
	[h m s]		[Mpc]	[pc arcsec^{-1}]	[mag]	[mag]	[arcsec]	[°]
(1)	(2)	(3)	(4)	(5)	(6)	(7)	(8)	(9)
NGC 3156	10 12 41.25	+03 07 45.69	21.8	106	12.05	−19.64	17.4	60
NGC 3245	10 27 18.39	+28 30 26.79	20.3	98	10.39	−21.15	25.1	57
NGC 3998	11 57 56.13	+55 27 12.92	13.7	66	11.04	−19.64	20.0	39
NGC 4578	12 37 30.56	+09 33 18.25	16.3	79	11.07	−20.00	32.4	45
NGC 4690	12 47 55.52	−01 39 21.83	40.2	195	12.26	−20.76	17.8	45
NGC 5687	14 34 52.40	+54 28 33.05	27.2	131	11.71	−20.46	22.9	51
NGC 6149	16 27 24.23	+19 35 49.91	37.2	180	12.65	−20.20	10.7	47
NGC 7457	23 00 59.93	+30 08 41.79	12.9	63	10.76	−19.79	36.3	58

Notes. Column (1): galaxy name. Columns (2), (3): right ascension and declination (J2000.0). Column (4): galaxy distance from Cappellari et al. (2011). Column (5): conversion factor from arcsec to parsec. Column (6): composite-model apparent *i*-band magnitude (cmodel) of the galaxy from SDSS. Column (7): absolute *i*-band magnitude of the galaxy. Column (8): circularized effective radius of the galaxy from Cappellari et al. (2011). Column (9): galaxy inclination $\theta_\epsilon = \arccos(1-\epsilon)$, where ε is galaxy ellipticity at $R_{\rm e,\,gal}$ from Krajnović et al. (2011).

Table 3. Characteristics of the *i*-band SDSS images of the sample galaxies.

Galaxy	Gain	RON	Sky	*FWHM*	β
	[e^- ADU^{-1}]	[e^-]	[ADU]	[arcsec]	
(1)	(2)	(3)	(4)	(5)	(6)
NGC 3156	5.2	14.5	144 ± 5	1.3	3.2
NGC 3245	6.6	16.4	186 ± 6	1.3	4.6
NGC 3998	4.6	13.0	177 ± 5	1.1	4.1
NGC 4578	4.9	10.4	160 ± 5	1.1	4.2
NGC 4690	6.6	16.4	206 ± 5	1.0	3.6
NGC 5687	6.6	16.4	224 ± 5	1.2	3.5
NGC 6149	4.9	10.4	124 ± 4	1.1	4.5
NGC 7457	6.6	16.4	211 ± 6	0.9	6.7

Notes. Column (1) galaxy name. Columns (2), (3): image gain and read-out provided by SDSS. Column (4): measured sky level and corresponding standard deviation. Columns (5), (6): *FWHM* and β parameter measured for the circular Moffat PSF.

disc to be elliptical, centred onto the galaxy center, and with constant position angle of the major axis and constant apparent axial ratio. GASP2D returns the best-fitting values of the structural parameters of the bulge (effective surface brightness $I_{\rm e}$, effective radius $r_{\rm e}$, Sérsic index n, position angle $PA_{\rm bulge}$, apparent axial ratio $q_{\rm bulge}$), disk (central surface brightness I_0, inner scalelength h, outer scalelength $h_{\rm o}$, break radius $r_{\rm break}$, position angle $PA_{\rm disk}$, apparent axial ratio $q_{\rm disk}$) with a χ^2 minimization by weighting the surface brightness of the image pixels according to the variance of the total observed photon counts due to the contribution of both galaxy and sky. The algorithm accounts also for photon noise, CCD gain and read-out noise, and image PSF and it excludes masked pixels from the minimization process.

We discriminated between elliptical and lenticular galaxies by using the logical filtering and statistical criteria given in Méndez-Abreu et al. (2018a) to decide whether to adopt or not a disc component to model the surface brightness distribution of the selected galaxies. The logical filter tells the difference between elliptical and lenticular galaxies by choosing the best-fitting model with a physical meaning. In fact, the lenticular galaxies are supposed to have both a bulge contributing most of the galaxy surface brightness in the inner regions and a disk dominating in the galaxy outskirts. The statistical significance of this analysis relies on the Bayesian information criterion (BIC; Schwarz 1978). Following the prescriptions of Simard et al. (2011), we adopted the *BIC* parameter

$$BIC = \chi^2 A_{\rm PSF} + k \ln\left(\frac{m}{A_{\rm PSF}}\right), \quad (1)$$

where k is the number of free parameters, m is the number of independent data points, and $A_{\rm PSF}$ is the size area of the FWHM$_{\rm PSF}$. As in Méndez-Abreu et al. (2018a), we took advantage of the simulated mock galaxies to set at $\Delta BIC = BIC(\text{bulge}) - BIC(\text{bulge + disk}) > -18$ the threshold that statistically sets the distinction between elliptical and lenticular galaxies. This led us to identify three elliptical galaxies, which we rejected.

We scrutinized the residual images obtained after subtracting the GASP2D model images of the remaining 19 *bona fide* lenticulars from their SDSS images to look for other components than bulge and disk (i.e. a main bar, large-scale spiral arms). Five galaxies showed a weak bar and/or a faint spiral structure and were discarded.

Under the assumption of circular and infinitesimally thin disk, we calculated the galaxy inclination $\theta = \arccos(q_{\rm disk})$, discarding six galaxies because of their high inclination.

Finally, we visually inspected the optical and near-infrared images of each of the remaining eight remaining galaxies available in the Hubble Space Telescope (*HST*) Science Archive to double check that they did not host nuclear bars, rings, or spiral arms.

We report the best-fitting structural parameters and corresponding errors for the eight sample galaxies, together with their ΔBIC values in Table 4. We derived the errors on the structural parameters of these galaxies by analysing the images of a sample of mock galaxies generated with Monte Carlo simulations and mimicking the available SDSS images following the procedure described in Costantin et al. (2017). We assumed the mock galaxies to be at a distance of 27 Mpc, which corresponds to the median distance of our sample galaxies.

We show in Fig. 1 the photometric decomposition of NGC 3156 as an example and present the results for the other sample galaxies in Fig. A1.

5 BULGE INTRINSIC SHAPE

We constrained the intrinsic shape of our sample bulges with the statistical method presented in Méndez-Abreu et al. (2010) and revised in Costantin et al. (2018) using our code galaXYZ written in

Table 4. Structural parameters of the sample galaxies.

Galaxy	μ_e	r_e	n	q_{bulge}	PA_{bulge}	μ_0	h	h_{out}	r_{break}	q_{disk}	PA_{disk}	B/T	ΔBIC
	[mag arcsec^{-2}]	[arcsec]			[°]	[mag arcsec^{-2}]	[arcsec]	[arcsec]	[arcsec]		[°]		
(1)	(2)	(3)	(4)	(5)	(6)	(7)	(8)	(9)	(10)	(11)	(12)	(13)	(14)	(15)
NGC 3156	20.06 ± 0.02	18.52 ± 0.05	4.7 ± 0.1	5.31 ± 0.04	0.580 ± 0.002	48.7 ± 0.1	18.68 ± 0.02	12.22 ± 0.07	19.6 ± 0.6	47 ± 1	0.495 ± 0.002	48.5 ± 0.2	0.16	103
NGC 3245	17.32 ± 0.01	16.42 ± 0.01	4.03 ± 0.02	1.52 ± 0.01	0.730 ± 0.001	175.7 ± 0.1	18.50 ± 0.01	20.61 ± 0.03	34.3 ± 0.1	78.4 ± 0.1	0.518 ± 0.001	176.5 ± 0.1	0.25	49
NGC 3998	17.31 ± 0.01	16.20 ± 0.02	5.40 ± 0.03	2.31 ± 0.01	0.838 ± 0.001	131.6 ± 0.1	19.10 ± 0.01	23.76 ± 0.06	40.7 ± 0.5	98.4 ± 0.8	0.790 ± 0.001	139.0 ± 0.1	0.42	2
NGC 4578	19.32 ± 0.01	18.13 ± 0.02	8.89 ± 0.06	2.71 ± 0.01	0.750 ± 0.001	32.5 ± 0.1	20.37 ± 0.01	32.51 ± 0.08	–	–	0.686 ± 0.001	30.6 ± 0.1	0.39	-16
NGC 4690	19.37 ± 0.02	17.91 ± 0.07	2.84 ± 0.09	4.52 ± 0.04	0.779 ± 0.002	148.1 ± 0.1	19.37 ± 0.02	10.4 ± 0.1	18.3 ± 0.5	28.6 ± 0.6	0.737 ± 0.002	149.2 ± 0.2	0.19	30
NGC 5687	19.01 ± 0.01	17.92 ± 0.03	6.67 ± 0.07	2.58 ± 0.01	0.686 ± 0.001	103.6 ± 0.1	20.16 ± 0.01	24.26 ± 0.08	–	–	0.622 ± 0.001	101.2 ± 0.1	0.40	-17
NGC 6149	18.79 ± 0.02	17.65 ± 0.07	3.0 ± 0.1	2.49 ± 0.03	0.691 ± 0.002	21.2 ± 0.1	19.50 ± 0.02	8.85 ± 0.05	–	–	0.660 ± 0.002	18.9 ± 0.2	0.39	0
NGC 7457	21.41 ± 0.01	19.92 ± 0.02	21.8 ± 0.1	4.86 ± 0.01	0.645 ± 0.002	128.9 ± 0.2	19.38 ± 0.06	28.01 ± 0.05	–	–	0.511 ± 0.001	125.0 ± 0.1	0.32	14

Notes. Column (1): galaxy name. Columns (2), (3), (4), (5), (6) and (7): surface brightness at effective radius, mean surface brightness within effective radius, effective radius, Sérsic index, apparent axial ratio, and position angle of the bulge, respectively. Columns (8), (9), (10) (11), (12), and (13): central surface brightness, inner scalelength radius, outer scalelength radius, break radius, apparent axial ratio, and position angle of the disk, respectively. Column (14): bulge-to-total luminosity ratio. Column (15): $\Delta BIC = BIC(\text{bulge}) - BIC(\text{bulge + disk})$.

IDL.[2] In summary, we first assumed that the bulge can be modelled by a triaxial ellipsoid with an equatorial axial ratio *B*/*A* and flattening *C*/*A* that shares both the same equatorial plane and center of the disk. Secondly, the disk component is considered to be an oblate ellipsoid with an intrinsic flattening described by a normal distribution with $\langle q_{0,\,\text{disk}}\rangle = 0.267 \pm 0.102$ (Rodríguez & Padilla 2013). It is worth noting that the inclination of our sample galaxies is in the range $25^\circ < \theta < 65^\circ$ for which the intrinsic shape of the bulge can be successfully constrained with galaXYZ (Costantin et al. 2018).

We show in Fig. 2 the probability distribution of *B*/*A* and *C*/*A* of the bulge in NGC 3156 as an example, while the remaining sample bulges are presented in Fig. A1. We list the most probable values of *B*/*A* and *C*/*A* of the sample bulges in Table 5.

As in Méndez-Abreu et al. (2018b), we discriminated bulges according to their intrinsic shape among oblate-triaxial and prolate-triaxial ellipsoids, following the description proposed by Franx, Illingworth & de Zeeuw (1991). Each class contains in-plane systems, which are flattened with respect to the disk equatorial plane, and off-plane systems, which are elongated along the polar axis. Special cases of this description include spherical ($A = B = C$), oblate axisymmetric ($B = A$), and prolate axisymmetric ($B = C$) spheroids.

Considering the intrinsic flattening of disks in nearby galaxies $\langle q_{0,\,\text{disk}}\rangle$, we calculated the probability of having a bulge as flattened as a disk component. First, we derived the probability $P(C/A < 0.369)_{\text{bulge}}$ for each sample bulge to be oblate ($B/A > 0.85$) and have a flattening $C/A < 0.369$ by taking into account the probability density function (PDF) of its axial ratios in the (*B*/*A*, *C*/*A*) diagram. This allows us to identify the more flattened bulges in our sample. Indeed, it is worth noting that this probability does not discriminate bulge types, but allows to characterize the more flattened systems comparing them with the intrinsic flattening of nearby disks. Secondly, we built up a statistical hypothesis test for discerning between disk-like bulges (null hypothesis H_0) and classical bulges (alternative hypothesis H_1) based on their *C*/*A* distribution. We considered as disk-like bulges the systems with an intrinsic flattening $(C/A)_{\text{bulge}}$ similar to that of nearby disks. We set the test statistic T_1, which calculates the shared area $A_{\text{disk-like}}$ between the PDF of the intrinsic flattening of nearby disks and the marginalized PDF over *B*/*A* of a sample bulge, where the full $A_{\text{disk-like}}$ is considered in the region $(C/A)_{\text{bulge}} < \langle q_{0,\,\text{disk}}\rangle$. To set the statistical limits of the hypothesis test, we generated a control sample of mock disk-like bulges, taking advantage of the PDFs of the bulge intrinsic shape in Costantin et al. (2018). For this purpose, we replicated and marginalized 5000 of those PDFs over *B*/*A* and centred each of them on a random value of $q_{0,\,\text{disk}}$ sampled from the normal disk distribution, i.e. we created a control sample of disk-like bulges with marginalized PDFs comparable with those measured with our galaXYZ code. Therefore, applying the test statistics to the control sample of mock disk-like bulges, we were able to set the limit that corresponds to a statistical test at 90 per cent confidence level. Thus, this allowed us to identify classical bulges (i.e. rejecting H_0 in favour of H_1) as those having $T_1 < 34$ per cent at 90 per cent confidence level (Table 5).

The results are given in Table 5. We found that NGC 6149 is the most flattened oblate bulge of our sample. Moreover, since it fails our statistical test, it is the only candidate to be disk-like according to its three-dimensional shape.

[2]Interactive Data Language is distributed by ITT Visual Information Solutions. It is available from http://www.ittvis.com.

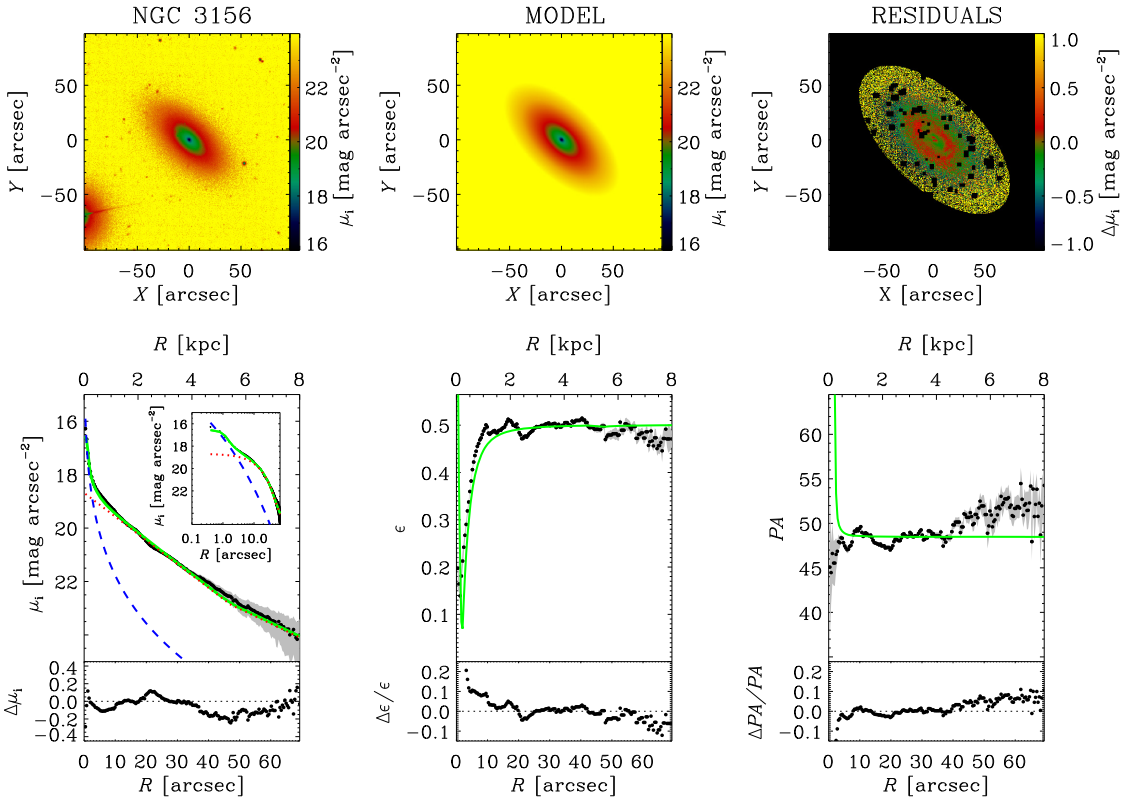

Figure 1. Two-dimensional photometric decomposition of the *i*-band image of the galaxy NGC 3156 as obtained from GASP2D. The upper panels (*from left to right*) show the map of the observed, modelled, and residual (observed−modelled) surface-brightness distributions. The field of view is oriented with North up and East left. The black areas in the residual image correspond to pixels excluded from the fit. The lower panels (*from left to right*) show the ellipse-averaged radial profile of surface brightness, position angle, and ellipticity measured in the observed (black dots with gray error bars) and seeing-convolved modelled image (green solid line) and their corresponding difference. The surface-brightness radial profiles of the best-fitting bulge (blue dashed line) and disk (red dotted line) are also shown in both linear and logarithmic scale for the distance to the center of the galaxy.

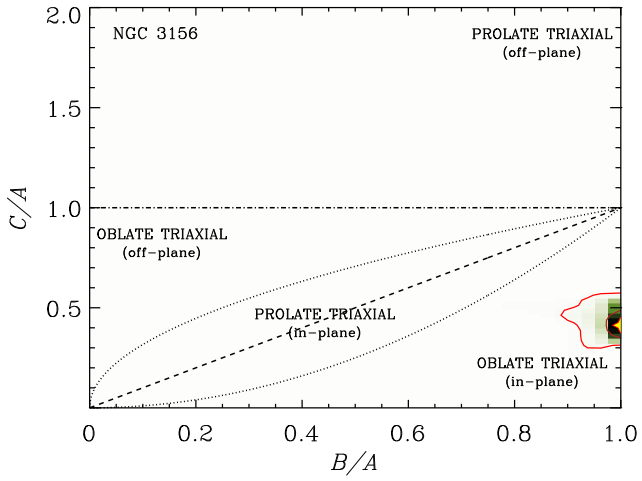

Figure 2. Distribution of the intrinsic axial ratios *B*/*A* and *C*/*A* of the bulge of NGC 3156. The yellow star corresponds to the most probable values of *B*/*A* and *C*/*A*. The inner and outer red solid contours respectively encompass the 68.3 per cent and 95.4 per cent of the realizations of (*B*/*A*, *C*/*A*) consistent with the geometric parameters of bulge and disk measured from our photometric decomposition. Different lines mark the regimes of oblate-triaxial (in-plane), oblate-triaxial (off-plane), prolate-triaxial (in-plane), and prolate-triaxial (off-plane).

Table 5. Most probable intrinsic shape of our sample bulges.

Galaxy (1)	*B*/*A* (2)	*C*/*A* (3)	$P(C/A < 0.369)_{\rm bulge}$ (4)	T_1 (5)
NGC 3156	1.00	0.41	15%	20%
NGC 3245	1.00	0.61	0%	4%
NGC 3998	0.94	0.59	15%	25%
NGC 4578	1.00	0.46	10%	20%
NGC 4690	1.00	0.46	10%	19%
NGC 5687	0.94	0.51	3%	18%
NGC 6149	0.96	0.36	45%	51%
NGC 7457	0.91	0.49	8%	22%

Notes. Column (1): galaxy name. Columns (2), (3): most probable intrinsic axial ratios of the bulge. Column (4): probability that the galaxy hosts an oblate bulge (*B*/*A* > 0.85) with an intrinsic flattening (*C*/*A*) less than 0.369. Column (5): T_1 test statistics as defined in Section 5.

6 INTEGRAL FIELD SPECTROSCOPY

For each sample galaxy, we computed the values of the bulge diagnostics listed in Section 2 and based on stellar kinematics and line-strength indices for each galaxy of the sample. To this aim, we took advantage of the two-dimensional maps of the line-of-sight (LOS) stellar velocity and velocity dispersion and of the equivalent width of the Mg_b and Fe_{5015} line-strength indices provided by the

Table 6. Kinematic parameters and line-strength indices for the sample galaxies.

Galaxy	$r_{25\,\mathrm{per\,cent}}$ [arcsec]	$\sigma_{r_e/10}$ [km s^{-1}]	σ_e [km s^{-1}]	$\langle v^2\rangle/\langle\sigma^2\rangle\vert_{r_{25\,\mathrm{per\,cent}}}$	$\langle v^2\rangle/\langle\sigma^2\rangle\vert_e$	Mg$_b$ [Å]	Mg$_{b,\,e}$ [Å]	Fe$_{5015}$ [Å]	Fe$_{5015,\,e}$ [Å]	γ
(1)	(2)	(3)	(4)	(5)	(6)	(7)	(8)	(9)	(10)	(11)
NGC 3156	2.28	71 ± 9	62 ± 8	0.11	0.16	1.50 ± 0.03	1.62 ± 0.06	3.65 ± 0.06	3.4 ± 0.1	-0.11
NGC 3245	7.03	229 ± 5	202 ± 3	0.19	0.16	4.10 ± 0.03	3.97 ± 0.03	5.23 ± 0.06	5.01 ± 0.08	-0.18
NGC 3998	12.93	282 ± 6	249 ± 4	0.22	0.16	4.67 ± 0.03	4.52 ± 0.05	1.39 ± 0.05	3.94 ± 0.09	-0.14
NGC 4578	16.03	111 ± 7	98 ± 6	0.32	0.33	4.36 ± 0.03	3.70 ± 0.09	5.59 ± 0.06	4.7 ± 0.2	-0.11
NGC 4690	2.94	127 ± 9	112 ± 8	0.02	0.02	3.31 ± 0.07	3.08 ± 0.08	4.5 ± 0.1	4.3 ± 0.2	-0.04
NGC 5687	12.14	193 ± 9	170 ± 6	0.20	0.18	4.28 ± 0.09	3.9 ± 0.1	5.4 ± 0.2	4.8 ± 0.2	-0.11
NGC 6149	4.68	111 ± 6	98 ± 5	0.36	0.28	3.38 ± 0.04	3.24 ± 0.05	4.64 ± 0.08	4.4 ± 0.1	-0.07
NGC 7457	7.62	70 ± 11	62 ± 10	0.06	0.33	2.93 ± 0.02	2.85 ± 0.09	5.02 ± 0.04	4.4 ± 0.2	-0.03

Notes. Column (1): galaxy name. Column (2): radius where the surface brightness contribution of the bulge exceeds that of the disk by $r_{25\,\mathrm{per\,cent}}$. Columns (3), (4): luminosity-weigthed values of LOS velocity dispersion within an elliptical aperture of semi-major axis $r_{e/10}$ and r_e, respectively. Column (5): luminosity-weighted value of v^2/σ^2 within a circular corona between $r_{\mathrm{min}} = FWHM_{\mathrm{PSF}}$ and $r_{\mathrm{max}} = r_{25\,\mathrm{per\,cent}}$. Column (6): luminosity-weighted value of v^2/σ^2 within an elliptical aperture of semi-major axis r_e. Columns (7), (9): luminosity-weigthed values of the Mg$_b$ and Fe$_{5015}$ line-strength indices within a circular aperture of 1.5 arcsec. Columns (8), (10): luminosity-weigthed values of the Mg$_b$ and Fe$_{5015}$ line-strength indices within an elliptical aperture of semi-major axis r_e. Column (11): logarithmic slope of the radial profile of the LOS velocity dispersion between $r_{\mathrm{min}} = FWHM_{\mathrm{PSF}}$ and $r_{\mathrm{max}} = r_{25\,\mathrm{per\,cent}}$.

ATLAS^{3D} survey[3] (see Emsellem et al. 2004; Cappellari et al. 2011; McDermid et al. 2015, for all details).

6.1 Stellar kinematics

For each galaxy, we calculated the luminosity-weighted LOS velocity dispersion within the bulge effective radius σ_e as

$$\sigma_e = \frac{\sum_{i=1}^{N} F_i \sigma_i}{\sum_{i=1}^{N} F_i}, \tag{2}$$

where σ_i is the LOS velocity dispersion and F_i is flux of i-th Voronoi bin within the elliptical aperture with semi-major axis r_e, axial ratio q_{bulge}, and position angle PA_{bulge}. We defined the central velocity dispersion σ_0 (diagnostics (II-1)$_C$) as the velocity dispersion within an elliptical aperture of radius $r_e/10$. We calculated it from σ_e as

$$\sigma_0 = \sigma_{r_e/10} = \sigma_e 10^{0.055\pm0.020}, \tag{3}$$

using the aperture correction derived for ETGs by Falcón-Barroso et al. (2017), who analysed of the stellar kinematics of the galaxies mapped by the Calar Alto Legacy Integral Field Area Survey (CALIFA) data release 3 (Sánchez et al. 2016).

Similarly to Fabricius et al. (2012), we calculated the luminosity-weighted $\langle v^2\rangle/\langle\sigma^2\rangle$ (diagnostics (I-4)$_{C,\,D}$) as

$$\left.\frac{\langle v^2\rangle}{\langle\sigma^2\rangle}\right|_{25\ \mathrm{per\ cent}} = \frac{\sum_{i=1}^{N} F_i v_i^2}{\sum_{i=1}^{N} F_i \sigma_i^2}, \tag{4}$$

where F_i is the flux of the i-th Voronoi bin within the circular corona with a minimum radius $r_{\mathrm{min}} = FWHM_{\mathrm{PSF}}$ to minimize the blurring effects of the PSF and a maximum radius $r_{\mathrm{max}} = r_{25\,\mathrm{per\,cent}}$ defined as the radius where the surface brightness contribution of the bulge exceeds that of the disk by 25 per cent, that is

$$I_e\, e^{b_n} e^{-\left(\frac{b_n\, r_{25\ \mathrm{per\ cent}}}{r_e}\right)^{1/n}} = 1.25\, I_{0,\,\mathrm{disk}}\, e^{-\left(\frac{r_{25\ \mathrm{per\ cent}}}{h}\right)}. \tag{5}$$

[3]The ATLAS^{3D} data are available at http://www-astro.physics.ox.ac.uk/atlas3d/.

For future reference, we also provided the luminosity-weighted $\langle v^2\rangle/\langle\sigma^2\rangle\vert_e$ value inside the bulge effective radius as

$$\left.\frac{\langle v^2\rangle}{\langle\sigma^2\rangle}\right|_e = \frac{\sum_{i=1}^{N} F_i v_{\mathrm{corr},i}^2}{\sum_{i=1}^{N} F_i \sigma_i^2}, \tag{6}$$

where $v_{\mathrm{corr},\,i}$ is the inclination-corrected velocity, σ_i is the LOS velocity dispersion, and F_i is the flux of the i-th Voronoi bin in the same elliptical aperture adopted for measuring σ_e (Binney 2005).

Finally, we derived the logarithmic slope γ of the velocity dispersion radial profile (diagnostics (I-4)$_{C,\,D}$) as

$$\gamma = \left\langle \frac{\mathrm{d}\log(\sigma)}{\mathrm{d}\log(r)} \right\rangle\Bigg|_{25\ \mathrm{per\ cent}}. \tag{7}$$

We made sure to avoid a dependence on the particular binning scheme of each kinematic data set by using a circular radial binning of five equally sized bins in $\log(r)$ (Fabricius et al. 2012).

We provide the values of $r_{25\,\mathrm{per\,cent}}$, $\sigma_{r_e/10}$, σ_e, $\langle v^2\rangle/\langle\sigma^2\rangle\vert_{25\ \mathrm{per\ cent}}$, $\langle v^2\rangle/\langle\sigma^2\rangle\vert_e$, and γ in Table 6. We show in Fig. 3 the stellar kinematics of NGC 3156 as example and show the remaining galaxies in Fig. A1.

It is worth noting that the field of view of the stellar kinematic maps typically encompasses one galaxy effective radius (Table 2) ensuring the full coverage of the bulge-dominated region. To give an idea of the bulge size, we overplot to the stellar kinematic maps the ellipse with semi-major axis r_e, axial ratio q_{bulge}, and position angle PA_{bulge} within which we calculated σ_e and $\langle v^2\rangle/\langle\sigma^2\rangle\vert_e$ as well as the circle with a radius of $r_{25\,\mathrm{per\,cent}}$. It results that if a galaxy shows a centrally-peaked velocity dispersion, the increase of the velocity dispersion is generally confined within the effective radius of the bulge (e.g. NGC 3245 and NGC 3998).

6.2 Line-strength indices

For each galaxy, we derived the luminosity-weighted central values of the line-strength indices Mg$_b$ and Fe$_{5015}$ within a circular aperture of 1.5-arcsec radius as

$$Index = \frac{\sum_{i=1}^{N} F_i Index_i}{\sum_{i=1}^{N} F_i}, \tag{8}$$

where $Index_i$ is the index equivalent width and F_i is flux of the i-th Voronoi bin within the selected aperture. This allows to apply of

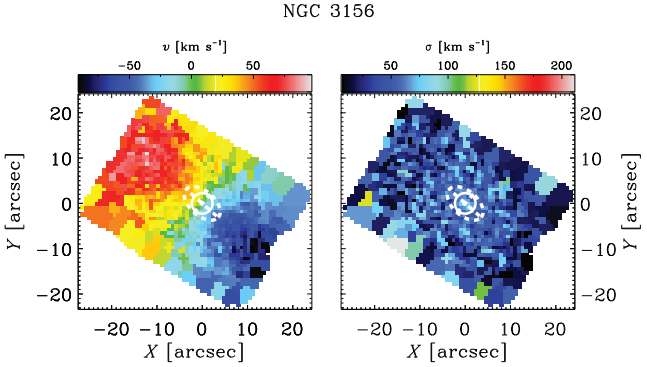

Figure 3. Two-dimensional map of the LOS velocity (*left panel*) and velocity dispersion (*right panel*) of the stellar component of NGC 3156. The white dashed line corresponds to the elliptical aperture with semi-major axis r_e, axial ratio q_{bulge}, and position angle PA_{bulge}. The white solid line marks the circle with radius $r_{25\,per\,cent}$. North is up and east is left.

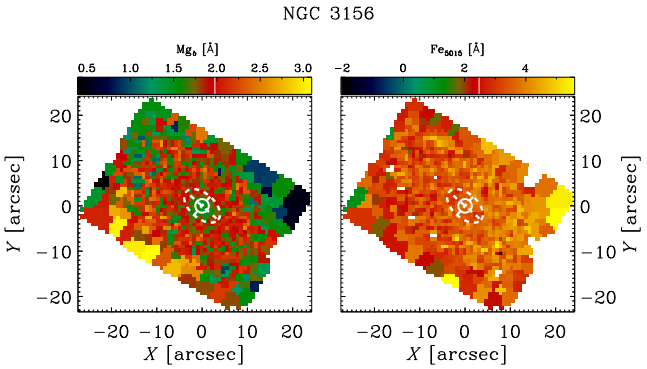

Figure 4. Two-dimensional map of the equivalent width of the Mg_b (*left panel*) and Fe_{5015} (*right panel*) line-strength indices of NGC 3156. The white dashed line corresponds to the elliptical aperture with semi-major axis r_e, axial ratio q_{bulge}, and position angle PA_{bulge}. The white solid line marks the circle with radius 1.5 arcsec. North is up and east is left.

the bulge diagnostics $(I\text{-}3)_D$ and $(II\text{-}3)_D$ related to the properties of their stellar populations.

Peletier et al. (2007) measured the line-strength indices within a circular aperture of 1.2-arcsec radius for 24 bulges of early-type spiral galaxies, while Ganda et al. (2007) measured them within a circular aperture of 1.5-arcsec radius for 18 bulges of late-type spiral galaxies. Fisher & Drory (2016) combined these measurements, stressing that no classical bulge has Mg_b<2.35 Å or Fe_{5015}<3.97 Å. It has to be strongly remarked that these thresholds were chosen once the bulges were already *a priori* classified as classical or disk-like by analyzing their visual morphological classification (diagnostics $(I\text{-}1)_{C,D}$) and/or Sérsic index (diagnostics $(I\text{-}2)_{C,D}$). For future reference, we also calculated the luminosity-weighted values $Mg_{b,e}$ and $Fe_{5015,e}$ of the line-strength indices Mg_b and Fe_{5015} in the same elliptical aperture adopted for measuring σ_e.

We listed the measured values of Mg_b, $Mg_{b,e}$, Fe_{5015}, and $Fe_{5015,e}$ of the sample galaxies in Table 6. We plot in Fig. 4 the two-dimensional map of the equivalent width of the Mg_b and Fe_{5015} line-strength indices of NGC 3156 as an example, while the remaining galaxies are shown in Fig. A1. We overplot the ellipse within which we calculated σ_e, as well as the circle with a radius of 1.5 arcsec. We found that the bulges of NGC 3156 and NGC 3998 have Fe_{5015}<3.95 Å, while only the bulge of NGC 3156 also presents Mg_b<2.35 Å.

Furthermore, we considered the Mg_b–σ_0 and Mg_b–Fe_{5015} relationships (diagnostics $(I\text{-}3)_D$) following Fisher & Drory (2016). We adopted as comparison sample the elliptical galaxies studied by Kuntschner et al. (2010, where $\sigma_0 = \sigma_{r_e/8}$) and the bulges from Peletier et al. (2007, where $\sigma_0 = \sigma_{1.2\,arcsec}$), and Ganda et al. (2007, where $\sigma_0 = \sigma_{1.5\,arcsec}$). We plot the two relationships with the best fit to the elliptical galaxies by Kuntschner et al. (2010) inferred from Fisher & Drory (2016) in Figs. 5 and 6, respectively.

We distinguished our sample bulges according to their Sérsic index between $n > 2$ and $n < 2$ as proposed by Fisher & Drory (2016) and we found that only the bulge of NGC 3156 is below the line that is supposed to separate the two bulge classes in both diagrams, with the bulge of NGC 7457 also meeting the disk-like requirement for the Mg_b–Fe_{5015} relation. The bulge of NGC 3998 is characterized by a very small value of Fe_{5015}. However, considering $Fe_{5015,e}$ it moves towards the Mg_b–Fe_{5015} relation.

7 SCALING RELATIONS

Following Costantin et al. (2017), we built the FPR (Djorgovski & Davis 1987; Cappellari et al. 2013), FJR (Faber & Jackson 1976; Falcón-Barroso et al. 2011), and KR (Kormendy 1977; Nigoche-Netro et al. 2008) using the photometric (r_e, $\langle\mu_e\rangle$, and $M_{bulge,i}$) and kinematic (σ_e) parameters of elliptical galaxies and bulges from Gadotti (2009) and Oh et al. (2011), respectively.

We combined the photometric and kinematic properties of our bulges to study their location in the FPR (Fig. 7; diagnostics $(III\text{-}2)_C$) and FJR (Fig. 8; diagnostics $(II\text{-}4)_D$), using the best-fitting relations provided by Costantin et al. (2017)

$$\log(r_e) = 0.99\log(\sigma_e) + 0.24\langle\mu_e\rangle - 6.46 \quad (9)$$

and

$$\log(\sigma_e) = -0.152\,(\pm0.003)M_i - 1.07\,(\pm0.07), \quad (10)$$

respectively. We found that none of our sample bulges is a low-σ outlier to either the FPR or the FJR. However, we noticed that our bulges are located systematically below the FPR best-fitting line and systematically above the FJR best-fitting line, even if they are consistent with their global trends within the errors. Only the bulge of NGC 3998 deviates more than 3σ in $\log\sigma_e$ from the FJR. We investigated the position of our sample bulges in the KR (Fig. 9; diagnostics $(II\text{-}1)_C$), taking advantage of the equation provided by Gadotti (2009)

$$\langle\mu_e\rangle = 1.74\,\log(r_e) + 19.17, \quad (11)$$

to separate classical from disk-like bulges. We found that all our bulges are consistent with the magnitude trend highlighted by Nigoche-Netro et al. (2008) and Costantin et al. (2017), discriminating between less and more massive bulges. As a consequence, using the KR to separate bulge types results in classifying less massive bulges as disk like. Therefore, in the low-mass regime even the most luminous bulges are supposed to be characterized by disk-like properties. In addition, we noticed that only the bulge of NGC 7457 is below the boundary line of the disk-like systems.

8 DISCUSSION

The observed properties of nearby bulges somehow preserve the relic of their formation and evolution. Thus, different observed

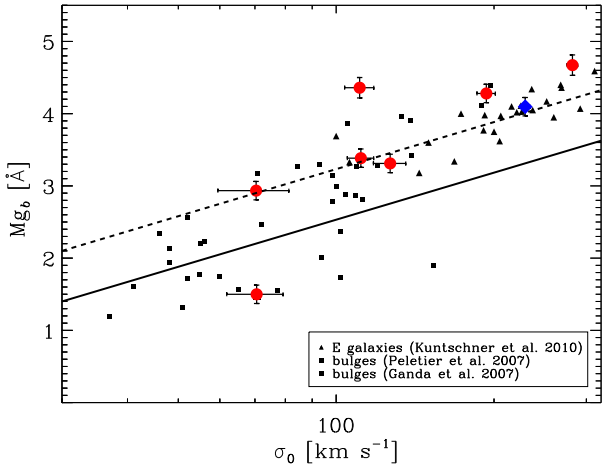

Figure 5. Mg$_b$–σ_0 relation for our sample bulges (large circles and diamonds) and the comparison sample of elliptical galaxies (small triangles) from Kuntschner et al. (2010) and bulges (small squares) from Peletier et al. (2007) and Ganda et al. (2007). Red and blue symbols mark the sample bulges with $n > 2$ and $n < 2$, respectively. The black dashed line is the best-fitting relation inferred by Fisher & Drory (2016) for the elliptical galaxies, while the black solid line corresponds to a deviation of 0.7 Å in Mg$_b$ from the best-fitting relation.

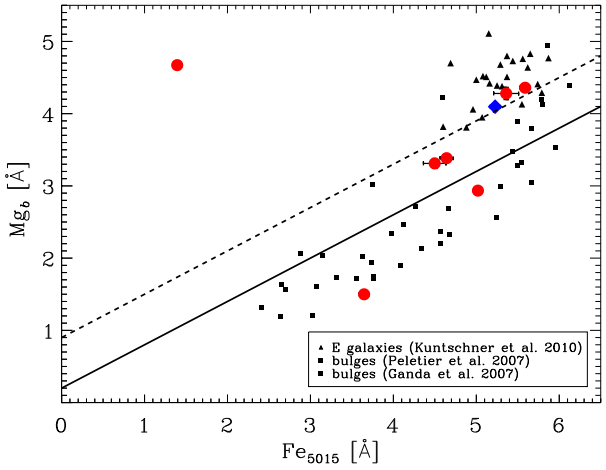

Figure 6. As in Fig. 5, but for the Mg$_b$–Fe$_{5015}$ relation.

properties are expected to be associated to various formation scenarios and, by consequence, to different bulge types. As proposed by Fisher & Drory (2016) and Kormendy (2016), the proper strategy would be to compare different diagnostics to take advantage of many observed properties. This is not usually done in the literature, since it is much easier to consider only one (or few) diagnostics, leading to misunderstandings due to misinterpretations of observational data and numerical results. For example, some recent numerical simulations have apparently challenged the current understanding of the relationships between the classification and formation of bulges. By fine-tuning simulation parameters, it has been possible to build classical bulges by disk instabilities and disk-like bulges from minor mergers (Keselman & Nusser 2012; Brooks & Christensen 2016; Weinzirl et al. 2009). However, the classical/disk-like bulge classification of these simulated galaxies is done using only the bulge Sérsic index as diagnostics. Thus, if different formation processes lead to the same observed property (as it results for the bulge Sérsic index), this makes the adopted diagnostics not fully reliable for discriminating the formation scenario of bulges and therefore not suitable for their classification.

In this context, the question is whether any, or any combination, of the diagnostics proposed by (Fisher & Drory 2016) could mark a distinction between the formation processes of bulges, or whether other new diagnostics could provide such a distinction. Thus, we compared the photometric, kinematic, and stellar population properties we derived for the sample bulges with the observational criteria given in Section 2 to identify classical (Table 7) and disk-like bulges (Table 8). The proposed diagnostics are potentially good in a statistical sense, while they result uncertain for individual galaxies.

Only the bulge of NGC 5687 can be unambiguously classified as classical, since it satisfies all the corresponding criteria and presents none of the characteristics for being disk-like. The remaining bulges show a more complex and therefore disputable behaviour. Nevertheless, we proposed to classify as classical also the bulges of NGC 3245, NGC 3998, and NGC 4578. Each of them actually misses only one of the criteria for being classical: the bulge of NGC 3254 has a small Sérsic index (diagnostics (I-2)$_C$), NGC 3998 does not follow the same correlations between line-strength indices as elliptical galaxies (diagnostics (I-3)$_C$), and NGC 4578 has a low central velocity dispersion (diagnostics (II-1)$_D$). However, performing a bulge classification using only one of these three diagnostics is quite controversial, because none of them is effective by itself to mark a clearcut separation between classical and disk-like bulges.

First, the Sérsic index is the most extensively adopted diagnostics to classify bulges (Fisher & Drory 2008; Neumann et al. 2017; Kruk et al. 2018), since the bimodal distribution of n is supposed to separate bulges in classical ($n > 2$) or disk-like ($n < 2$). However, a physical explanation for this bimodal distribution and for the empirical boundary line $n = 2$ is not well understood yet (Fisher & Drory 2016). Moreover, many authors pointed out that the Sérsic index is prone to misclassifications (e.g. Graham & Worley 2008; Méndez-Abreu et al. 2018a). It is known that mergers can build bulges with $n < 2$ (Eliche-Moral et al. 2011; Querejeta et al. 2015) and low-luminosity elliptical galaxies have $n < 2$ or even $n \sim 1$ (Davies et al. 1988; Young & Currie 1994). Thus, considering as disk-like all the systems with low Sérsic index leads to a heterogeneous collection of bulges with different formation scenarios, rather than singling out only the bulges built up from disk material during long-lasting processes.

Secondly, the Mg$_b$ and Fe$_{5015}$ line-strength indices and their interplay in the Mg$_b$–Fe$_{5015}$ relation are supposed to provide a constraint for the properties of the stellar population of bulges. However, their interpretation leads to contradictory outcomes, which are mostly inconsistent with those obtained from the analysis of the other photometric or kinematic parameters. We ascribed this to the variety of techniques adopted to analyse data and measure the line-strength indices of the comparison sample. Indeed, Fisher & Drory (2016) combined information from both Peletier et al. (2007) and Ganda et al. (2007), even if they measured the equivalent width of the line-strength indices within different circular apertures of radius 1.2 and 1.5 arcsec, respectively. This does not guarantee a fair comparison of different bulges, since their physical size is not appropriately taken into account. Furthermore, the separation of classical and disk-like bulges in the Mg$_b$–σ_0 and Mg$_b$–Fe$_{5015}$ relations (diagnostics (I-3)$_D$) was completely based on empirical results, once classical and disk-like bulges were already identified according to their visual morphological classification (diagnostics (I-1)$_{C,D}$) and/or Sérsic index (diagnostics (I-2)$_{C,D}$). We found that NGC 3156 hosts the only bulge in our sample falling in the disk-like region defined from the

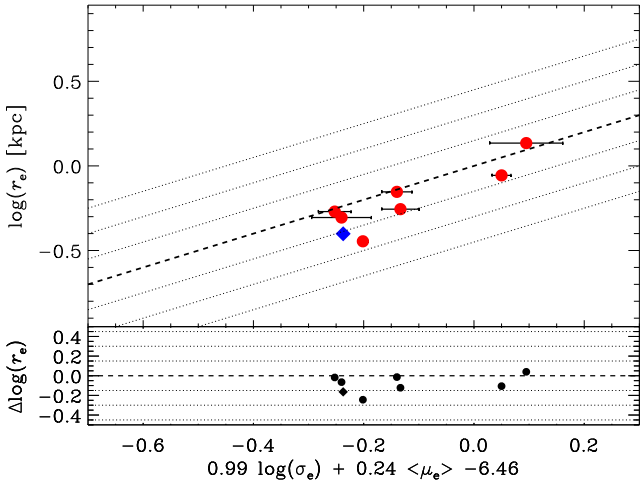

Figure 7. Fundamental plane relation for our sample bulges. Red and blue symbols mark the sample bulges with $n > 2$ and $n < 2$, respectively. The black dashed line corresponds to the best-fitting relation derived by Costantin et al. (2017). The black dotted lines show the 1 rms, 2 rms, and 3 rms deviation in log (r_e) regions, respectively.

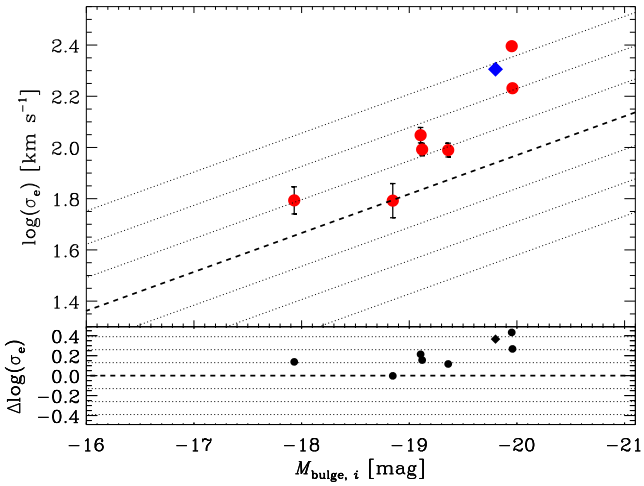

Figure 8. As in Fig. 7, but for the Faber-Jackson relation and with the rms deviation in log (σ_e) from the best fitting-relation.

Mg$_b$–σ_0 and Mg$_b$–Fe$_{5015}$ relations, with the bulge of NGC 7457 also meeting the disk-like requirement for the Mg$_b$–Fe$_{5015}$ relation. Nevertheless, both bulges have $n > 2$, whereas the bulge of NGC 3245 has $n < 2$ and it is consistent with the expected trends of classical bulges.

Finally, the stellar kinematics might be a good gauge of the nature of disk-like bulges, since they are supposed to preserve the properties of the disks from which they formed. However, we refrained from considering as disk-like all the bulges with a low-velocity dispersion. Indeed, the velocity dispersion of the bulge only partially characterizes its dynamical status being just a good proxy for the mass in dispersion-dominated systems. The fact that only three out of eight bulges in our sample (NGC 3245, NGC 3998, and NGC 5687) show a central velocity dispersion $\sigma_{r_e/10} > 130$ km s^{-1} does not rule out the possibility of labelling other sample bulges as classical. Costantin et al. (2017) investigated a sample of small bulges ($\sigma_e \simeq 50$ km s^{-1}) of late-type spirals and found they follow the

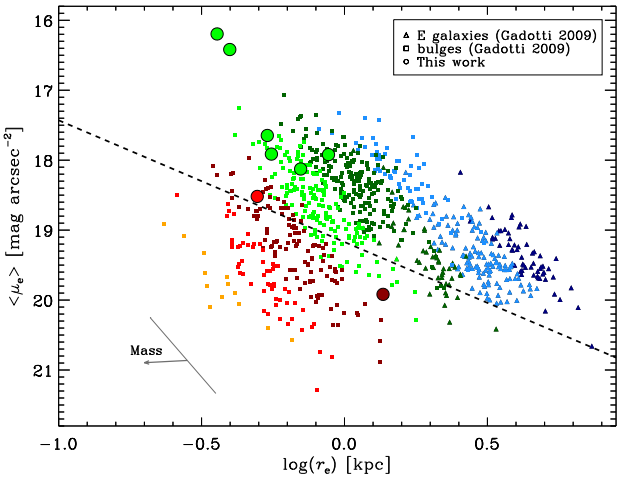

Figure 9. Kormendy relation for the bulges of our (large circles) and comparison sample from Gadotti (2009, small triangles: elliptical galaxies, small squares: bulges). The bulges are divided according to their absolute magnitude in the following bins: $M_i < -22$ mag (dark blue), $M_i = [-22, -21]$ mag (light blue), $M_i = [-21, -20]$ mag (dark green), $M_i = [-20, -19]$ mag (light green), $M_i = [-19, -18]$ mag (dark red), $M_i = [-18, -17]$ mag (light red), and $M_i = [-17, -16]$ mag (orange). The black dashed line separates classical from disk-like bulges according to Gadotti (2009). The black dash-dotted line gives the slope of the relation for the magnitude bin $M_i = [-20, -19]$ mag, while the arrow indicates the trend for decreasing masses (Nigoche-Netro, Ruelas-Mayorga & Franco-Balderas 2008).

same scaling relations of ellipticals, massive bulges, and compact early-type galaxies so they cannot be classified as disc-like systems.

It is worth noting that the failure of the photometric (n) and kinematic (σ,$\langle v^2\rangle/\langle\sigma^2\rangle$, and γ) diagnostics in giving the same classification for our sample bulges is not surprising. Controversial results have been obtained when these diagnostics were combined to classify bulges for which accurate photometric and kinematic measurements were available. Méndez-Abreu et al. (2018a) found no statistically significant correlation between the v/σ and n regardless of projection effects by analysing a sample of lenticular galaxies. Falcón-Barroso et al. (2003) studied early-type disk galaxies and argued that n is not related to γ. Recently, Tabor et al. (2017) have performed a spectrophotometric bulge-disk decomposition of three lenticular galaxies, showing that their bulges are pressure-supported systems despite they having $n \sim 1$ and some degree of rotation. On the contrary, Fabricius et al. (2012) claimed that bulges with $n < 2$ of galaxies ranging from lenticular to late-type spiral galaxies are characterized by an increased rotational support. The differences probably arise from the fact that bulges of late-type spiral galaxies are more consistently rotation-dominated and have a lower velocity dispersion than bulges of lenticular galaxies, whose formation process is more complex (Bekki 1998; Governato et al. 2009; Méndez-Abreu et al. 2018a).

The position of our sample bulges in the FPR, FJR, and KR confirmed the recent findings of Costantin et al. (2017) on scaling relations for elliptical galaxies and bulges. They claimed that there is a single population of galaxy spheroids that follow the same FPR (Fig. 7) and FJR (Fig. 8) and argued that the mass is responsible for the smooth transition in the photometric and kinematic properties from less to more massive bulges.

Photometric, kinematic, and line-strength diagnostics contradict each other for the bulges of NGC 3156, NGC 4690, NGC 6149, and NGC 7547 making them difficult to be classified. For this

Table 7. Classification criteria of classical bulges.

Galaxy	Morph.	n	Line-str. rel.		γ	σ_0	FPR	Classical bulge	3D shape
	$(I–1)_C$	$(I–2)_C$	$(I–3)_C$		$(I–4)_C$	$(II–1)_C$	$(III–1)_C$		
(1)	(2)	(3)	(4)		(5)	(6)	(7)	(8)	(9)
NGC 3156	yes	yes	no	no	yes	no	yes	?	yes
NGC 3245	yes	no	yes	yes	yes	yes	yes	yes	yes
NGC 3998	yes	yes	yes	yes	yes	yes	yes	yes	yes
NGC 4578	yes	yes	yes	yes	yes	no	yes	yes	yes
NGC 4690	yes	yes	yes	yes	no	no	yes	?	yes
NGC 5687	...	yes	yes	yes	yes	yes	yes	yes	yes
NGC 6149	...	yes	yes	yes	no	no	yes	?	no
NGC 7457	yes	yes	yes	no	no	no	yes	?	yes

Notes. Column (1): galaxy name. Column (2): morphological features from *HST* images (... = unavailable *HST* image). Column (3): Sérsic index $n > 2$. Column (4): consistency with Mg_b–$Fe_{5015}$and Mg_b–σ_0 correlations, respectively. Column (5): velocity dispersion gradient $\gamma < -0.1$. Column (6): central velocity dispersion $\sigma_0 > 130\,\mathrm{km\ s^{-1}}$. Column (7): consistency with FPR. Column (8): bulge classification according to the observational diagnostics listed in Cols. (2)-(7), and explained in Section2 (? = uncertain). Column (9): thick oblate spheroid: either $B/A > 0.85$ & $C/A > 0.37$ or $B/A < 0.85$ & any C/A.

Table 8. Classification criteria of disk-like bulges.

Galaxy	Morph.	n	Line-str. rel.		Kinematics		KR	Line-str. ind.		FJR	Disk-like bulge	3D shape
	$(I–1)_D$	$(I–2)_D$	$(I–3)_D$		$(I–4)_D$		$(II–1)_D$	$(II–3)_D$		$(II–4)_D$		
(1)	(2)	(3)	(4)		(5)	(6)	(7)	(8)	(9)	(10)	(11)	(12)
NGC 3156	no	no	yes	yes	no	no	no	yes	yes	no	?	no
NGC 3245	no	yes	no	no	no	no	no	no	no	no	no	no
NGC 3998	no	no	no	no	no	no	no	no	yes	no	no	no
NGC 4578	no	no	no	no	no	no	no	no	no	no	no	no
NGC 4690	no	no	no	no	no	yes	no	no	no	no	?	no
NGC 5687	...	no	no	no	no	no	no	no	no	no	no	no
NGC 6149	...	no	no	no	yes	yes	no	no	no	no	?	yes
NGC 7457	no	no	yes	no	no	yes	yes	no	no	no	?	no

Notes. Column (1): galaxy name. Column (2): morphological features from *HST* images (... = unavailable *HST* image). Column (3): Sérsic index $n < 2$. Column (4): deviation from Mg_b–$Fe_{5015}$and Mg_b–σ_0 correlations, respectively. Columns (5), (6): $\langle v^2\rangle/\langle\sigma^2\rangle|r_{25\mathrm{per\,cent}} \geq 0.35$ and velocity dispersion gradient $\gamma \geq -0.1$, respectively. Column (7): low surface brightness outlier from KR. Columns (8), (9): line-strength indices (Mg_b <2.35 Å Fe_{5015} <3.95 Å). Column (10): low-σ outliers from FJR. Column (11): bulge classification according to the observational diagnostics listed in Cols. (2)-(7), and explained in Section2 (? = uncertain). Column (12): flattened oblate spheroid: $B/A > 0.85$ & $C/A < 0.37$.

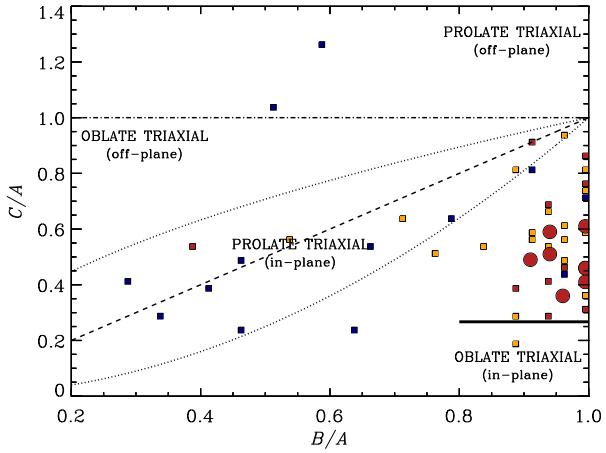

Figure 10. As in Fig. 2, but for the sample bulges (large circles) and the bulges of unbarred galaxies studied by Costantin et al. (2018, small squares). Red, yellow, and blue symbols mark galaxies classified as S0, Sa–Sb, and Sc–Sdm, respectively. The thick solid black line corresponds to $\langle q_{0,\,\mathrm{disk}}\rangle$ in Rodríguez & Padilla (2013). The bulges of NGC 4578 and NGC 4690 share the same position in the (B/A, C/A) diagram.

reason, we propose to add a piece of information by considering the bulge three-dimensional shape as a possible proxy to distinguish their nature. Our analysis suggests that all sample bulges are oblate spheroids, but only the bulge of NGC 6149 cannot be considered as classical at 90 per cent C.L. (Table 5). Therefore, we conclude that bulges of NGC 3156, NGC 4690, and NGC 7547 are most likely classical rather than disk-like, while NGC 6149 is consider to host a possible disk-like bulge. As shown in Section 5, we claim that our ability to constrain the bulge intrinsic shape is not limited to identify only classical bulges. For comparison, we found that a few oblate bulges from the sample of unbarred galaxies ranging from S0 to Sdm and taken from the CALIFA survey in Costantin et al. (2018) cannot be classified as classical since they fail our statistical test analysis (Fig. 10).

9 CONCLUSIONS

Analysing the SDSS (Ahn et al. 2012) and ATLAS^{3D} (Cappellari et al. 2011; McDermid et al. 2015) data sets, we derived the photometric and spectroscopic properties of a sample of *bona fide* unbarred lenticular galaxies in order to understand whether they host a classical or a disc-like bulge applying the observational diagnostics proposed by Fisher & Drory (2016).

We obtained the photometric diagnostics (n) of the sample bulges by performing a two-dimensional photometric decomposition of the SDSS i-band images. We derived the kinematic (σ, $\langle v^2\rangle/\langle\sigma^2\rangle$, and γ) and line-strength (Mg_b and Fe_{5015}) diagnostics within different apertures. In addition, we combined the line-strength indices and velocity dispersion in the Mg_b–Fe_{5015} and Mg_b–σ_0 relations. Finally, we used the photometric and kinematic parameters to investigate the location of the sample bulges in FPR, FJR, and KR built for elliptical and bulges.

We noticed that only sometimes the proposed diagnostics are successful in identifying classical bulges (Tables 7 and 8). As a matter of fact, the kinematic and line-strength diagnostics provided no clear identification for half of the sample bulges. This remains true also when we compared the classification based on the photometric and line-strength diagnostics. We derived the intrinsic shape of the sample bulges. All of them turned out to be thick oblate spheroids, but only NGC 6149 could be considered to most likely host a disk-like bulge. We concluded that all the other bulges could be classified as classical. We pointed out that the intrinsic shape of bulges, which reflects the violent/secular evolution of galaxies, could add a piece of information in characterizing the bulge types, unveiling extreme cases and tracing a continuity among them. The analysis of the bulge shape cannot replace a full investigation of all the observed properties. But, it can be adopted to guess the shape of the gravitational potential in the centre of nearby galaxies without the demand of a full orbital analysis, which is still not clear whether it would be able to completely solve this problem (Zhu et al. 2018a,b).

Despite the low number statistics, but taking advantage of the careful selection of our sample, we concluded that the common practice of applying the observational diagnostics by Fisher & Drory (2016) for distinguishing bulge types (based on an *a priori* classification according to their morphology and/or Sérsic index) has to be carefully reconsidered. We remarked that, even if each diagnostics looks well motivated in terms of distinct formation paths of bulges, their calibration and interplay might result in controversial findings. This is a pilot project, which requires further analysis with MUSE spectroscopy and *HST* imaging to improve the data spatial resolution (e.g. Gadotti et al. 2015), and a larger sample that includes barred galaxies and spirals to fine-tune the diagnostics. We propose the intrinsic three-dimensional shape as a new possible diagnostics to separate classical and disk-like bulges. This is a powerful tool to unveil the actual nature of galactic bulges and truly address the demography of classical and disc-like bulges in the nearby universe.

ACKNOWLEDGEMENTS

We would like to thank the anonymous referee for the suggestions that helped us to improve the way we presented our results, Dimitri Gadotti for his comments about the photometric and kinematic analysis, and Alessio Boletti for his remarks about the probabilistic tests. E.M.C. and L.M. acknowledge financial support from Padua University through grants DOR1699945, DOR1715817, DOR1885254, and BIRD164402/16. JMA acknowledge support from the Spanish Ministerio de Economia y Competitividad (MINECO) for the grant AYA2013-43188-P. L.C. is grateful to the Instituto de Astrofísica de Canarias for hospitality while this paper was in progress. This research also made use of the NASA/IPAC Extragalactic Database (NED) which is operated by the Jet Propulsion Laboratory, California Institute of Technology, under contract with the National Aeronautics and Space Administration (http://ned.ipac.caltech.edu/). We acknowledge the use of SDSS data (http://www.sdss.org).

REFERENCES

Aguerri J. A. L., Balcells M., Peletier R. F., 2001, A&A, 367, 428
Ahn C. P. et al., 2012, ApJS, 203, 21
Athanassoula E., 2005, MNRAS, 358, 1477
Bekki K., 1998, ApJ, 502, L133
Binney J., 2005, MNRAS, 363, 937
Bournaud F., 2016, in Laurikainen E., Peletier R., Gadotti D., eds, Galactic Bulges. Springer, Berlin, p. 355
Brooks A., Christensen C., 2016, in Laurikainen E., Peletier R., Gadotti D., eds, Galactic Bulges. Springer, Berlin, p. 317
Cappellari M. et al., 2011, MNRAS, 413, 813
Cappellari M. et al., 2013, MNRAS, 432, 1709
Cappellari M., 2016, ARA&A, 54, 597
Carollo C. M., Ferguson H. C., Wyse R. F. G., 1999, The Formation of Galactic Bulges. Cambridge Univ. Press, Cambridge
Costantin L., Méndez-Abreu J., Corsini E. M., Morelli L., Aguerri J. A. L., Dalla Bontà E., Pizzella A., 2017, A&A, 601, A84
Costantin L., Méndez-Abreu J., Corsini E. M., Eliche-Moral M. C., Tapia T., Morelli L., Dalla Bontà E., Pizzella A., 2018, A&A, 609, A132
Davies J. I., Phillipps S., Cawson M. G. M., Disney M. J., Kibblewhite E. J., 1988, MNRAS, 232, 239
Djorgovski S., Davis M., 1987, ApJ, 313, 59
Eggen O. J., Lynden-Bell D., Sandage A. R., 1962, ApJ, 136, 748
Eliche-Moral M. C., González-García A. C., Balcells M., Aguerri J. A. L., Gallego J., Zamorano J., Prieto M., 2011, A&A, 533, A104
Emsellem E. et al., 2004, MNRAS, 352, 721
Emsellem E. et al., 2011, MNRAS, 414, 888
Erwin P. et al., 2015, MNRAS, 446, 4039
Erwin P., Debattista V. P., 2017, MNRAS, 468, 2058
Faber S. M., Jackson R. E., 1976, ApJ, 204, 668
Fabricius M. H., Saglia R. P., Fisher D. B., Drory N., Bender R., Hopp U., 2012, ApJ, 754, 67
Falcón-Barroso J. et al., 2011, MNRAS, 417, 1787
Falcón-Barroso J. et al., 2017, A&A, 597, A48
Falcón-Barroso J., Balcells M., Peletier R. F., Vazdekis A., 2003, A&A, 405, 455
Fernández Lorenzo M. et al., 2014, ApJ, 788, L39
Fisher D. B., Drory N., 2008, AJ, 136, 773
Fisher D. B., Drory N., 2010, ApJ, 716, 942
Fisher D. B., Drory N., 2016, in Laurikainen E., Peletier R., Gadotti D., eds, Galactic Bulges. Springer, Berlin, p. 41
Franx M., Illingworth G., de Zeeuw T., 1991, ApJ, 383, 112
Gadotti D. A., 2009, MNRAS, 393, 1531
Gadotti D. A., Seidel M. K., Sánchez-Blázquez P., Falcón-Barroso J., Husemann B., Coelho P., Pérez I., 2015, A&A, 584, A90
Ganda K. et al., 2007, MNRAS, 380, 506
Governato F. et al., 2009, MNRAS, 398, 312
Graham A. W., Worley C. C., 2008, MNRAS, 388, 1708
Hopkins P. F., Cox T. J., Younger J. D., Hernquist L., 2009, ApJ, 691, 1168
Hubble E., 1943, ApJ, 97, 112
Jedrzejewski R. I., 1987, MNRAS, 226, 747
Kent S. M., 1986, AJ, 91, 1301
Keselman J. A., Nusser A., 2012, MNRAS, 424, 1232
Kormendy J., 1977, ApJ, 217, 406
Kormendy J., 1993, in Dejonghe H., Habing H. J., eds, IAU Symposium Vol. 153, Galactic Bulges. Kluwer Acad Pub, Dordrecht, p. 209
Kormendy J., 2016, in Laurikainen E., Peletier R., Gadotti D., eds, Galactic Bulges. Springer, Berlin, p. 431
Kormendy J., Kennicutt R. C., Jr., 2004, ARA&A, 42, 603
Krajnović D. et al., 2011, MNRAS, 414, 2923
Kruk S. J. et al., 2018, MNRAS, 473, 4731
Kuntschner H. et al., 2010, MNRAS, 408, 97
Laurikainen E., Salo H., Buta R., 2005, MNRAS, 362, 1319
McDermid R. M. et al., 2006, MNRAS, 373, 906
McDermid R. M. et al., 2015, MNRAS, 448, 3484
Méndez-Abreu J. et al., 2017, A&A, 598, A32
Méndez-Abreu J. et al., 2018a, MNRAS, 474, 1307

Méndez-Abreu J., Aguerri J. A. L., Corsini E. M., Simonneau E., 2008a, A&A, 478, 353
Méndez-Abreu J., Corsini E. M., Debattista V. P., De Rijcke S., Aguerri J. A. L., Pizzella A., 2008b, ApJ, 679, L73
Méndez-Abreu J., Simonneau E., Aguerri J. A. L., Corsini E. M., 2010, A&A, 521, A71
Méndez-Abreu J., Debattista V. P., Corsini E. M., Aguerri J. A. L., 2014, A&A, 572, A25
Méndez-Abreu J., Costantin L., Aguerri J. A. L., de Lorenzo-Cáceres A., Corsini E. M., 2018b, MNRAS, preprint (arXiv:1805.09481)
Mishra P. K., Wadadekar Y., Barway S., 2017, MNRAS, 467, 2384
Moffat A. F. J., 1969, A&A, 3, 455
Neumann J. et al., 2017, A&A, 604, A30
Nigoche-Netro A., Ruelas-Mayorga A., Franco-Balderas A., 2008, A&A, 491, 731
Oh K., Sarzi M., Schawinski K., Yi S. K., 2011, ApJS, 195, 13
Pagotto I. et al., 2017, AN, 338, 841
Peletier R. F. et al., 2007, MNRAS, 379, 445
Pohlen M., Trujillo I., 2006, A&A, 454, 759
Querejeta M., Eliche-Moral M. C., Tapia T., Borlaff A., Rodríguez-Pérez C., Zamorano J., Gallego J., 2015, A&A, 573, A78
Renzini A., 1999, in Carollo C. M., Ferguson H. C., Wyse R. F. G., eds, The Formation of Galactic Bulges. Cambridge University Press, Cambridge, p. 9
Rodríguez S., Padilla N. D., 2013, MNRAS, 434, 2153
Sánchez S. F. et al., 2016, A&A, 594, A36
Sarzi M. et al., 2013, MNRAS, 432, 1845
Schwarz G., 1978, Annals of Statistics, 6, 461
Scott N. et al., 2013, MNRAS, 432, 1894
Sérsic J. L., 1968, Atlas de Galaxias Australes. Observatorio Astronomico de Cordoba, Cordoba
Simard L., Mendel J. T., Patton D. R., Ellison S. L., McConnachie A. W., 2011, ApJS, 196, 11
Tabor M., Merrifield M., Aragón-Salamanca A., Cappellari M., Bamford S. P., Johnston E., 2017, MNRAS, 466, 2024
Vaghmare K., Barway S., Mathur S., Kembhavi A. K., 2015, MNRAS, 450, 873
Weinzirl T., Jogee S., Khochfar S., Burkert A., Kormendy J., 2009, ApJ, 696, 411
Young C. K., Currie M. J., 1994, MNRAS, 268, L11
Zhu L. et al., 2018a, Nature Astronomy, 2, 233
Zhu L., van de Ven G., Méndez-Abreu J., Obreja A., 2018b, MNRAS

APPENDIX A: ADDITIONAL FIGURES

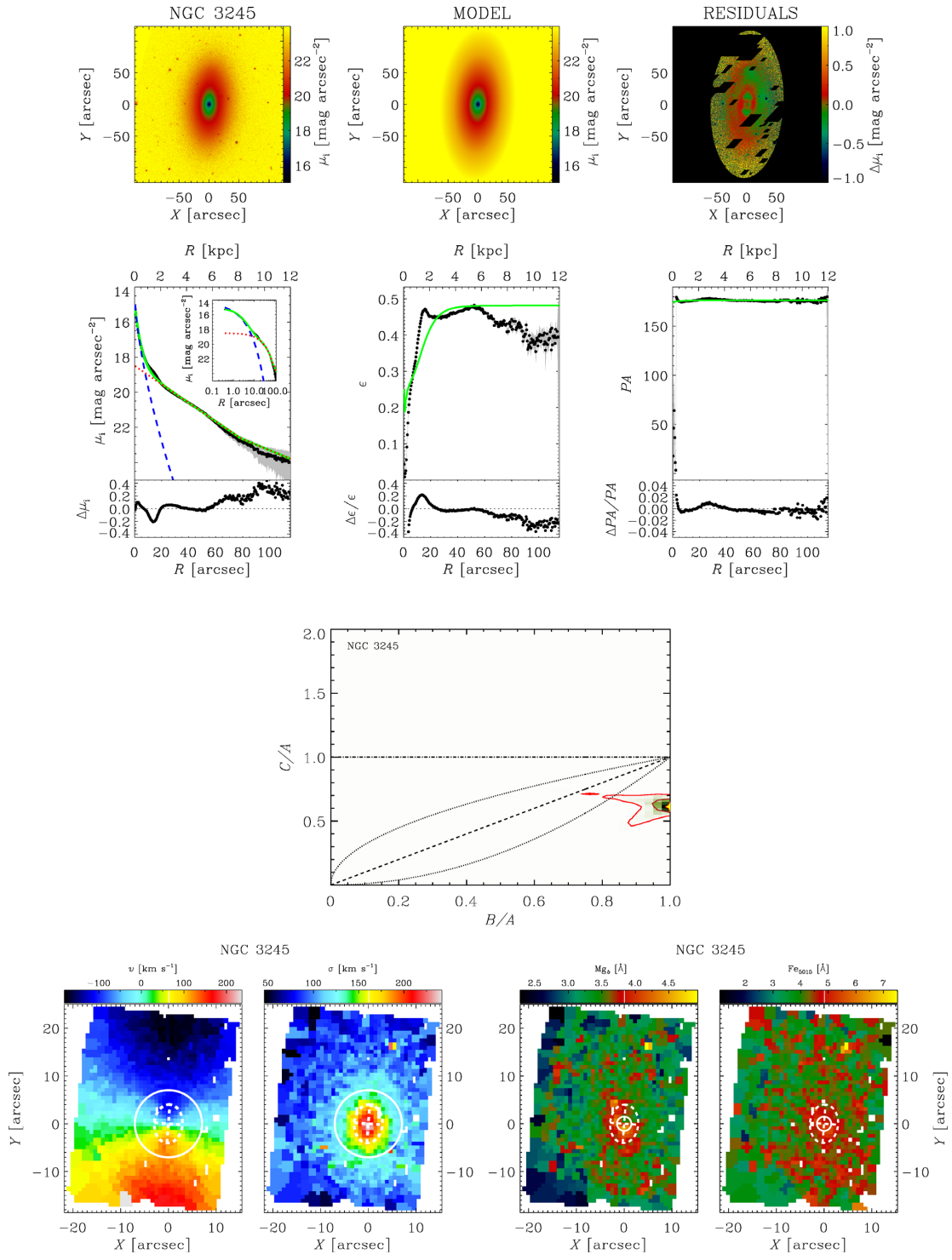

Figure A1. Two-dimensional photometric decomposition (*top panels*, as in Fig. 1), distribution of the intrinsic axial ratios of the bulge (*middle panels*, as in Fig. 2), two-dimensional maps of the stellar kinematics (*bottom left panels*, as in Fig. 3) and line-strength indices (*bottom right panels*, as in Fig. 4) of the sample galaxies, except for NGC 3156. The galaxy name is given in each plot.

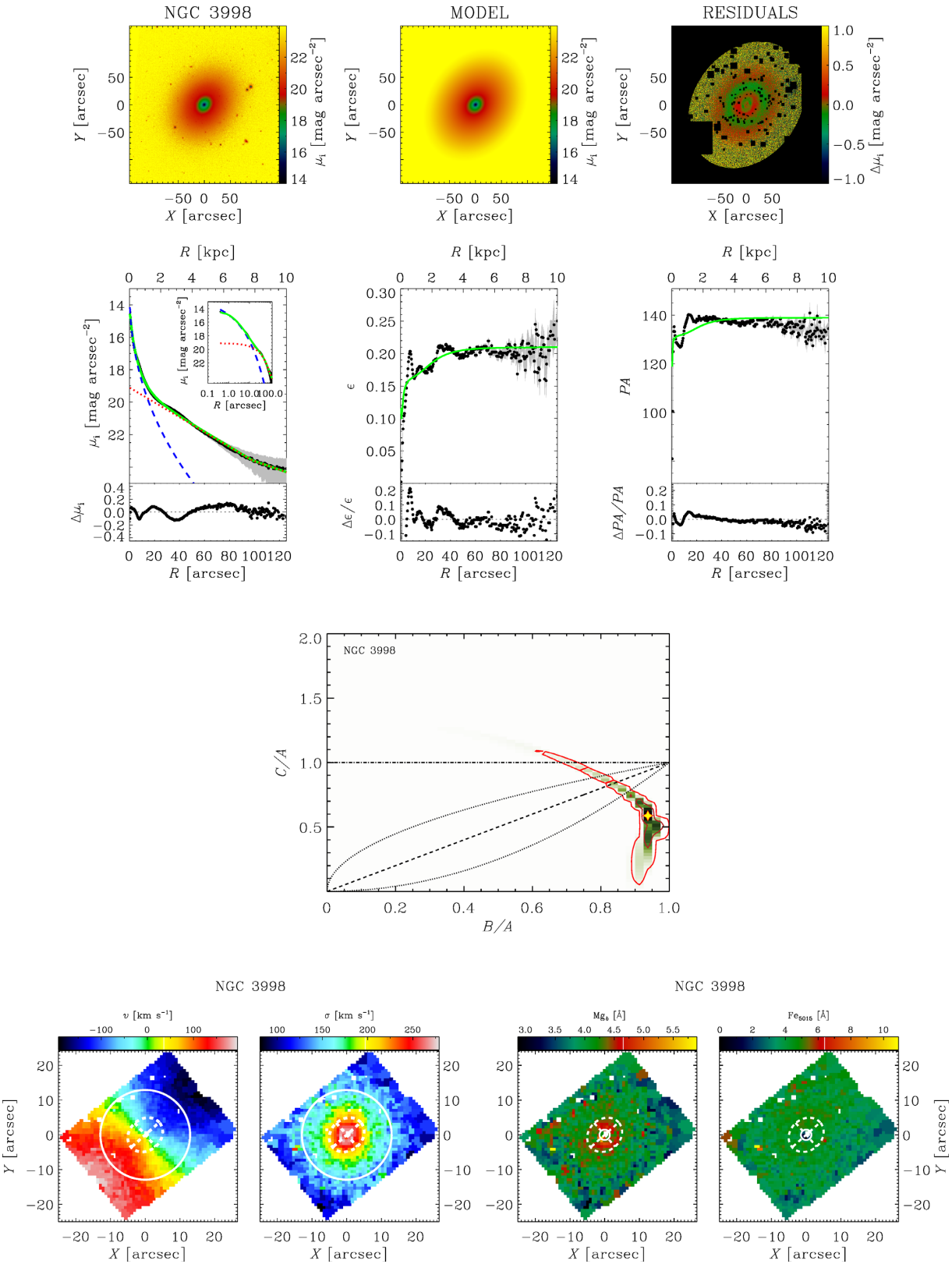

Figure A1. continue.

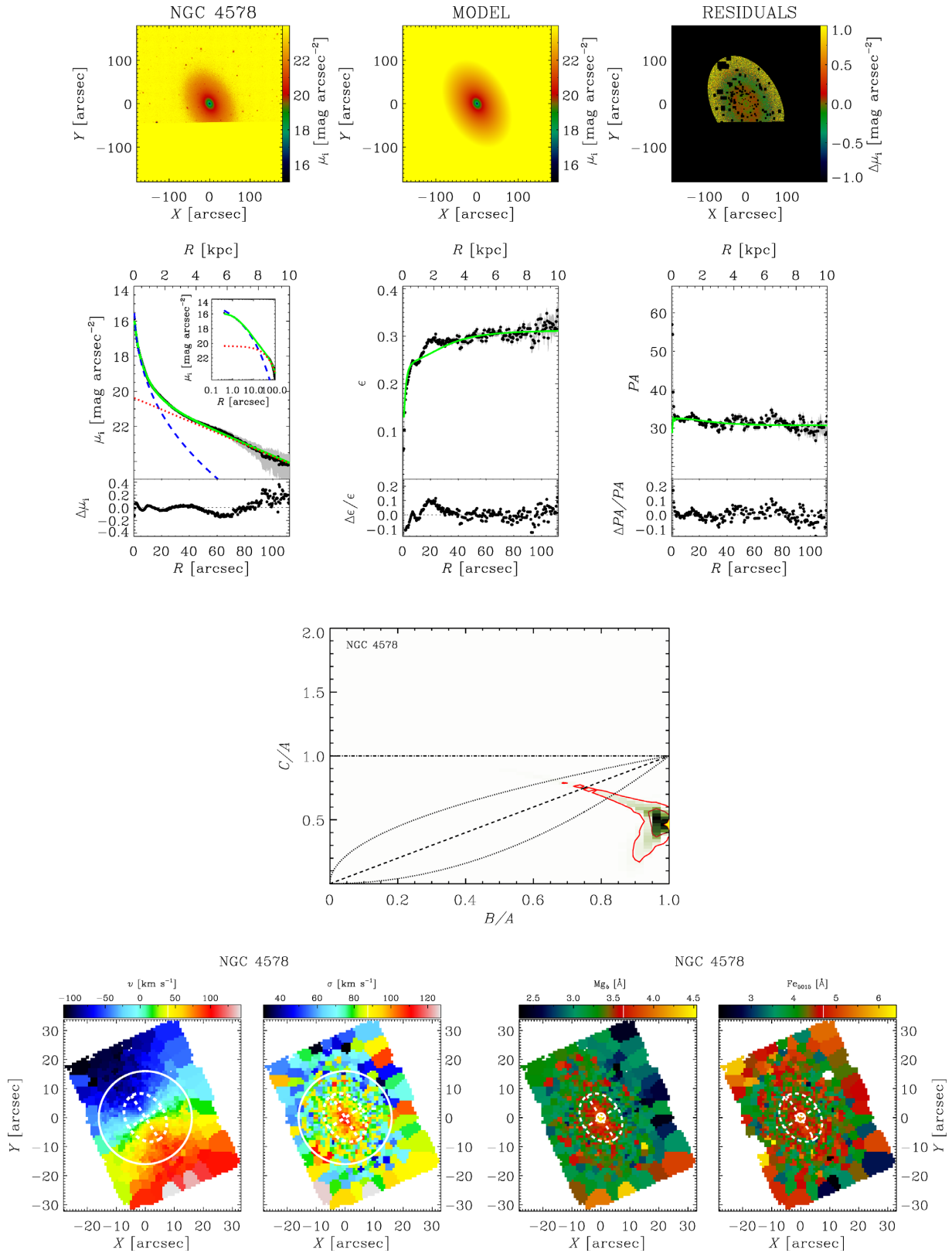

Figure A1. continue.

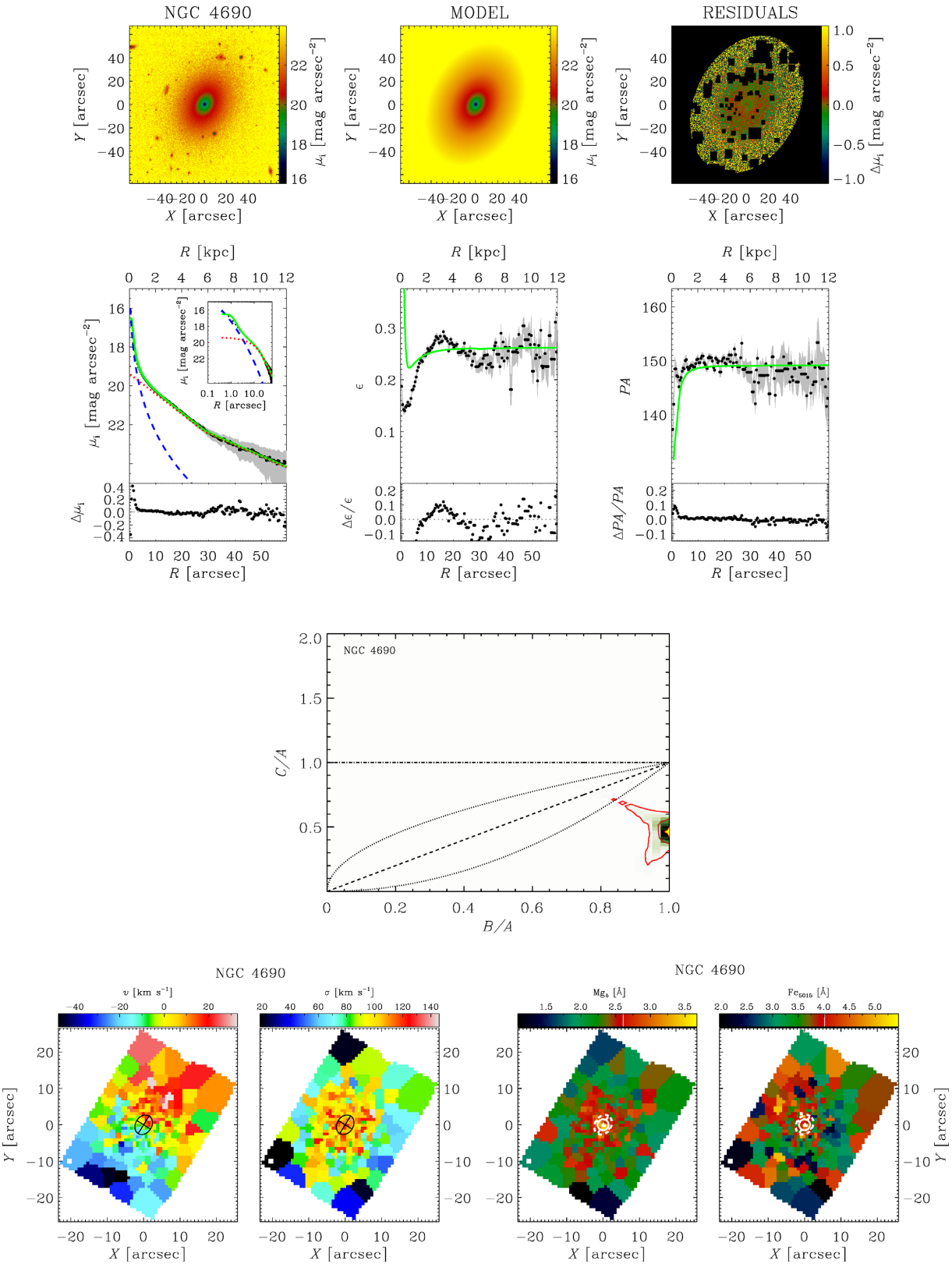

Figure A1. continue.

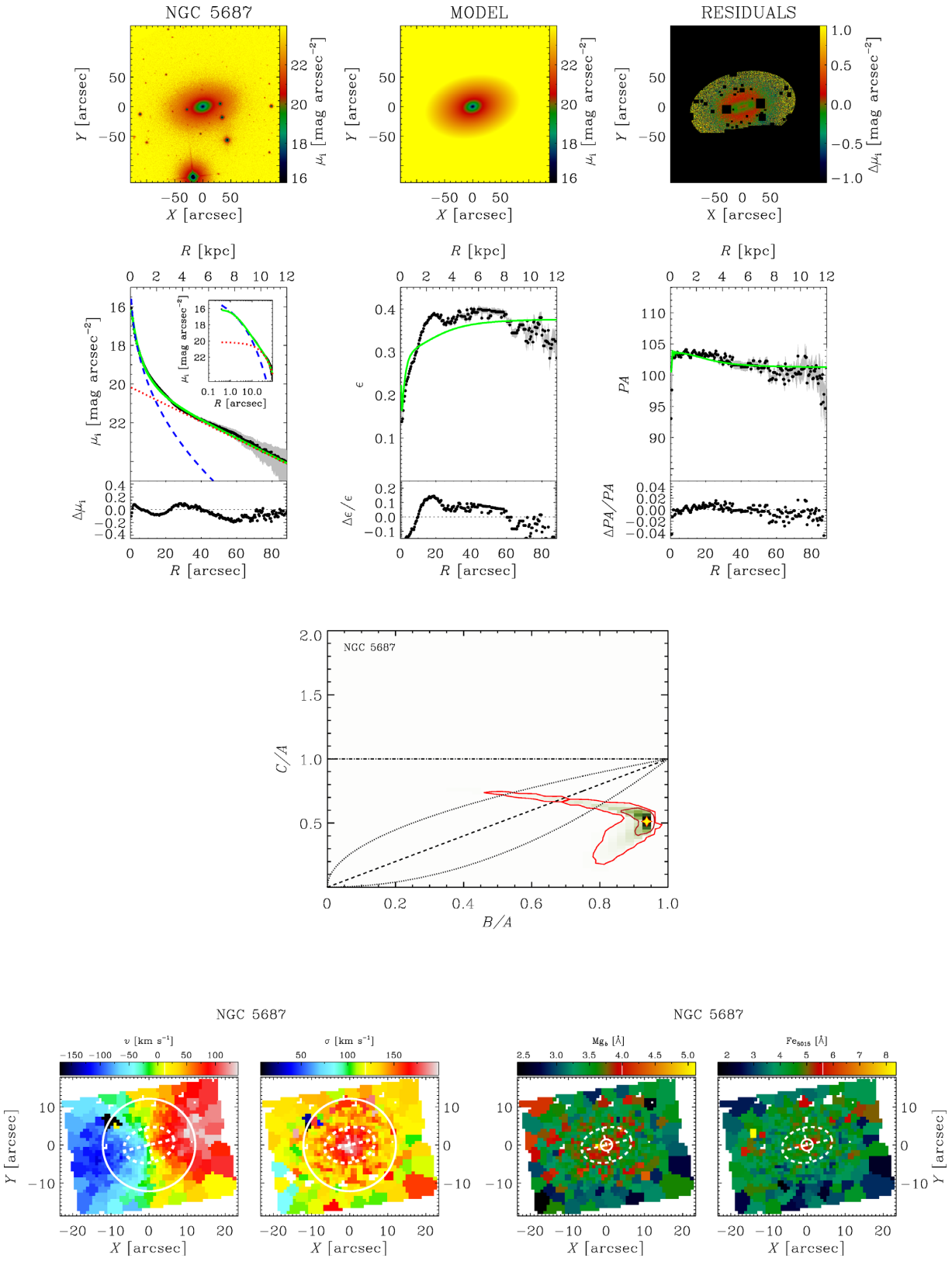

Figure A1. continue.

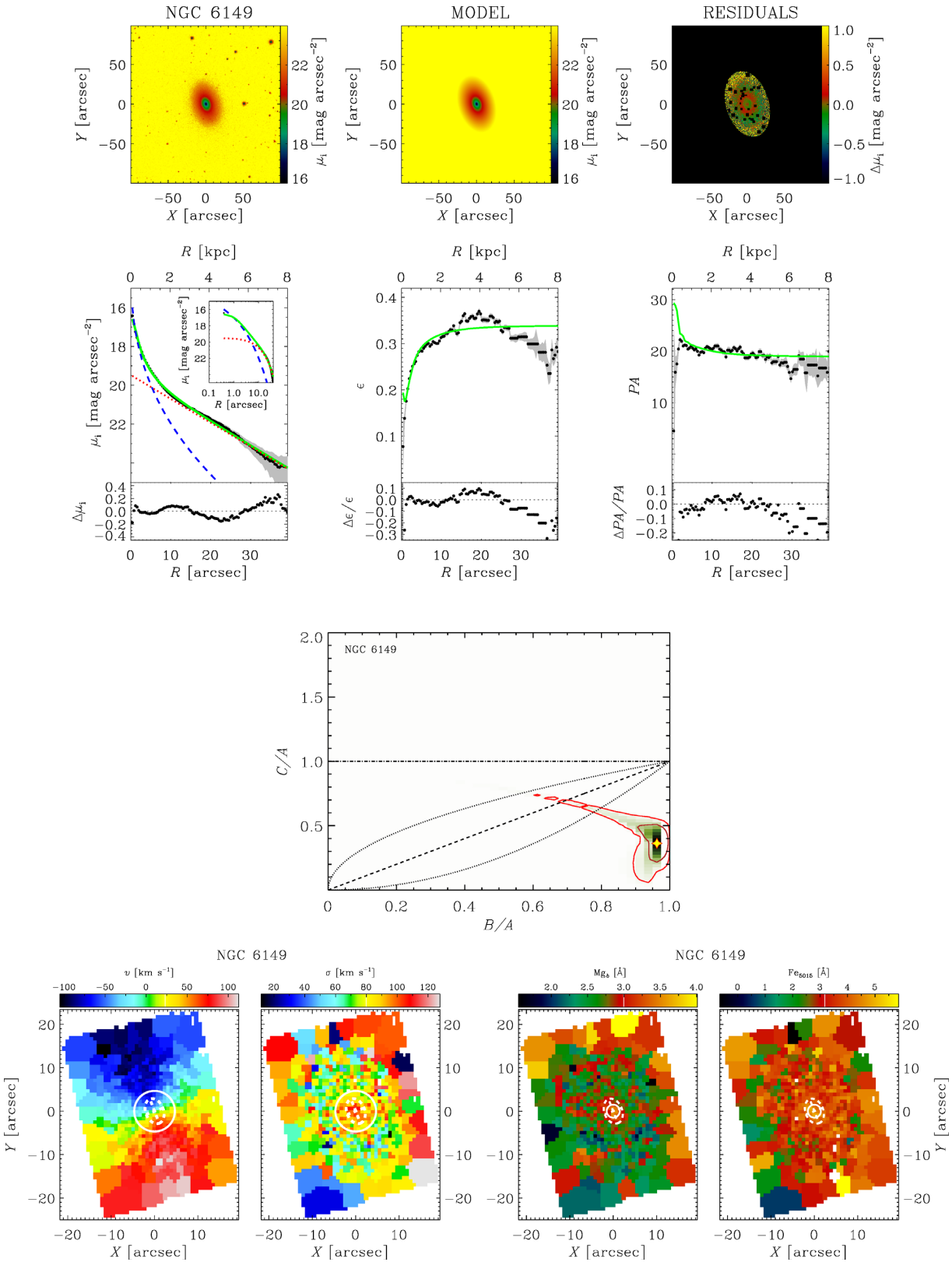

Figure A1. continue.

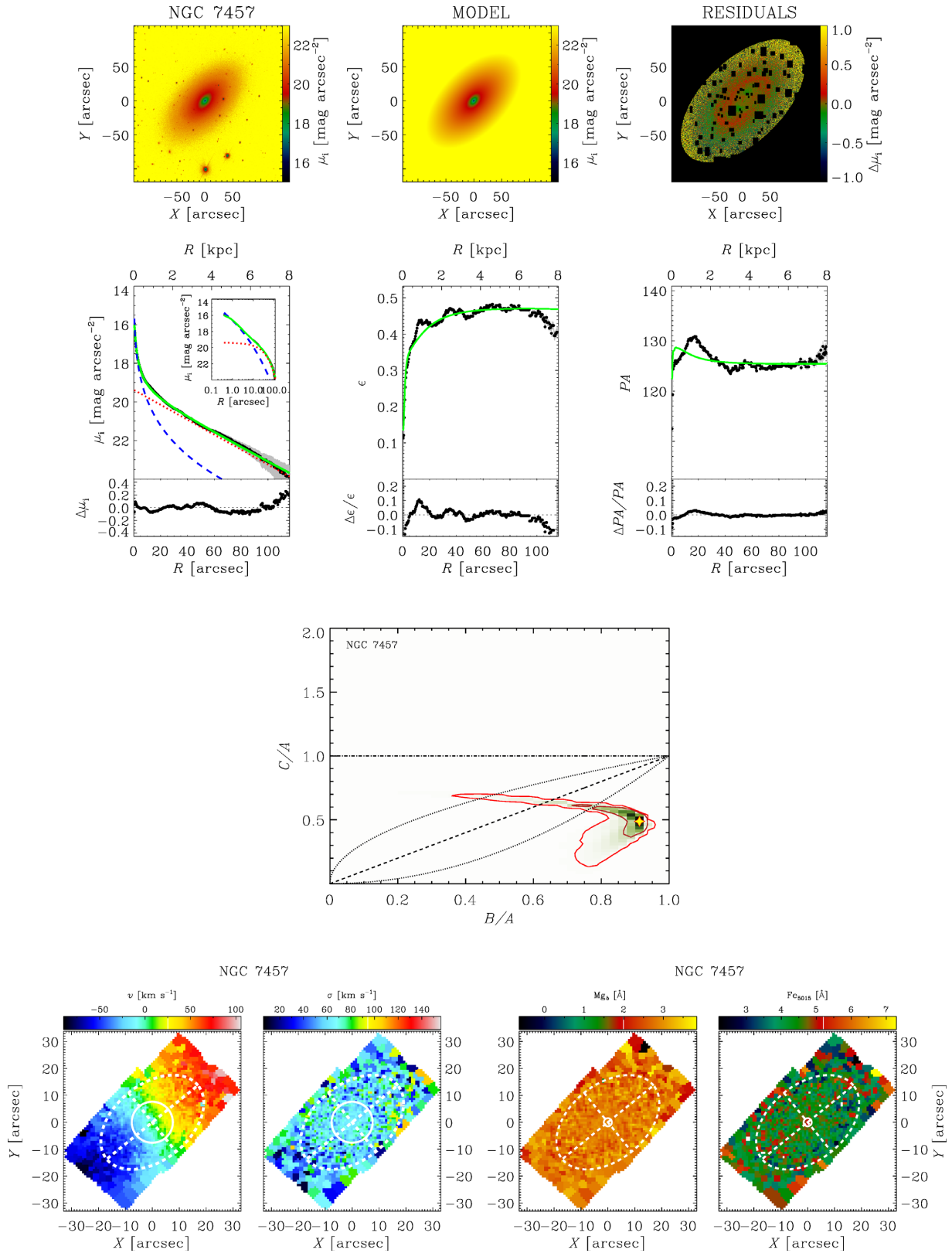

Figure A1. continue.

This paper has been typeset from a TEX/LATEX file prepared by the author.